

CM²



MAGAZINE

第 61 期



南方科技大学海洋磁学中心主编

<https://cm2.sustech.edu.cn/>

创刊词

海洋是生命的摇篮，是文明的纽带。地球上最早的生命诞生于海洋，海洋里的生命最终进化成了人类，人类的文化融合又通过海洋得以实现。人因海而兴。

人类对海洋的探索从未停止。从远古时代美丽的神话传说，到麦哲伦的全球航行，再到现代对大洋的科学钻探计划，海洋逐渐从人类敬畏崇拜幻想的精神寄托演变成可以开发利用与科学研究的客观存在。其中，上个世纪与太空探索同步发展的大洋科学钻探计划将人类对海洋的认知推向了崭新的纬度：深海（deep sea）与深时（deep time）。大洋钻探计划让人类知道，奔流不息的大海之下，埋藏的却是亿万年的地球历史。它们记录了地球板块的运动，从而使板块构造学说得到证实；它们记录了地球环境的演变，从而让古海洋学方兴未艾。

在探索海洋的悠久历史中，从大航海时代的导航，到大洋钻探计划中不可或缺的磁性地层学，磁学发挥了不可替代的作用。这不是偶然，因为从微观到宏观，磁性是最基本的物理属性之一，可以说，万物皆有磁性。基于课题组的学科背景和对海洋的理解，我们对海洋的探索以磁学为主要手段，海洋磁学中心因此而生。

海洋磁学中心，简称 CM^2 ，一为其全名“Centre for Marine Magnetism”的缩写，另者恰与爱因斯坦著名的质能方程 $E = MC^2$ 对称，借以表达我们对科学巨匠的敬仰和对科学的不懈追求。

然而科学从来不是单打独斗的产物。我们以磁学为研究海洋的主攻利器，但绝不仅限于磁学。凡与磁学相关的领域均是我们关注的重点。为了跟踪反映国内外地球科学特别是与磁学有关的地球科学领域的最新研究进展，海洋磁学中心特地主办 CM^2 Magazine，以期与各位地球科学工作者相互交流学习、合作共进！

“海洋孕育了生命，联通了世界，促进了发展”。21世纪是海洋科学的时代，由陆向海，让我们携手迈进中国海洋科学的黄金时代。

目录

研究进展.....	1
蔡书慧等-PNAS: 东南亚考古磁学结果揭示地磁场负异常.....	1
文献速递.....	8
1. 放射性核素的摇摆匹配揭示早全新世大太阳极小期在格林兰和西欧存在气候不同步震荡.....	8
2. 西太平洋副热带高压与亚洲夏季风并置形成了亚热带东亚降水	12
3. 自生胶黄铁矿指示新西兰 Hikurangi 边缘含天然气水合物的沉积物中甲烷扩散 16	
4. 来自伊豆-小笠原-马里亚纳弧发育早期的高度难熔地幔源区的玄武岩.....	19
5. 东亚下方的水平板片及其柔和的动力学响应	21
6. 东亚夏季风陆地的水汽源-汇网络与相关大气转向.....	26
7. 测试海水中钙浓度的变化对浮游有孔虫中其他元素/钙比的影响: 利用培养实验.....	29
8. 地中海东部地磁场异常的发生方向: 来自塞浦路斯的新数据与突变方向	31
9. 地磁场强度与白垩纪正极性超时: 来自哥斯达黎加的新结果	33
10. 由湖泊沉积物重建全新世以来东格陵兰岛 Renland 冰盖的演化史.....	36
11. Ranau 和 Telupid(马来西亚沙巴洲)超基性岩锆石 U-Pb 年龄和 Lu-Hf 同位素: 对东南亚的构造演化的启示.....	38
12. 对风化的玄武岩岩脉进行地磁测量和磁化率测绘揭示土壤蠕变与扰动	40

研究进展

蔡书慧等-PNAS: 东南亚考古磁学结果揭示地磁场负异常

地磁场是地球的基本物理场之一，起源于地球液态外核，能够反映地球内部结构和运动状态，同时环绕在地球周围，保护着地球宜居环境。研究地磁场变化规律在认识地球深部动力机制、地表过程和环境、现代地磁场特征和变化趋势等方面具有重要意义。大量不同时空分布的高质量观测数据是全面认识地磁场区域和全球变化特征的必要条件。近现代的卫星观测数据满足这一要求，但覆盖时间短。考古磁学可以把地磁场观测记录回溯至近几千年甚至全新世，在建立地磁场区域和全球模型方面具有重要贡献。然而，目前全球考古磁学数据分布严重不均，大部分数据集中在欧洲和中东地区，北半球低纬度地区和南半球数据稀少，制约了对地磁场形态特征和变化规律的准确认识。

东南亚地区正是上述全球数据匮乏区之一。中科院地质与地球物理研究所蔡书慧副研究员联合美国加州大学圣迭戈分校 Lisa Tauxe 教授、美国芝加哥伊利诺大学考古学家 Mitch Hendrickson 副教授、澳大利亚 ^{14}C 定年专家 Quan Hua 博士和柬埔寨考古项目组专家等，对位于东南亚柬埔寨北部的一处古代冶铁遗址（Tonle Bak）开展了考古磁学研究，获得了该地区首批地磁场全矢量数据。研究结果不仅大大改善了全球考古磁学数据结构，还记录到地磁场负异常，为认识低纬度地区地磁场特征及核幔边界结构提供了新思路，并为今后相关区域考古磁学工作提出了新方向。

Tonle Bak 遗址位于著名的吴哥窟古城以东~135 km（图 1a），考古调查结果显示它所在的 Phnom Dek 地区很可能为吴哥王朝扩张时期很重要的铁金属供应地，在该地区发现了十几处冶铁遗址，本文采样区 Tonle Bak 遗址是其中一处（图 1b）。本研究对出土的 3 个冶炼窑址（Furnace1, Furnace2, Furnace3）和 3 个发掘沟堆积剖面（Trench1, Trench3, Trench4）系统采集了定向样品（窑底或窑壁固结烧土）、非定向样品（烧土、吹风管、炉渣）和碳屑（图 2）。碳屑的 ^{14}C 定年结果将遗址年龄范围限定为公元 1034-1391 年。窑址定向样品记录的地磁场方向结果结合邻近地区已发表数据显示地磁场方向在公元 1200-1300 年间发生突变（图 3a），即使变化速率下限也高于该地区现代地磁场方向平均变化速率。同时样品强度结果显示公元 1100-1300 年地磁场强度存在不对称“V”形变化，最低值出现在公元 1200-1300 年（图 3b），与方向结果对应。

Tarduno 等 (2015) 在非洲南部的考古磁学研究发现类似的地磁异常, 公元 1300 年左右地磁场方向突变伴随地磁场强度降低, 研究区位于非洲下部低剪切速度地幔异常体 (LLSVP) 陡峭边界的正上方, 因此作者将这一磁异常归因于核幔边界处地形异常引起的磁通量溢出 (magnetic flux expulsion) 产生的反向涡流 (reversal flux patch)。本研究获得的柬埔寨考古磁学结果与非洲南部结果非常相似, 且两个研究区都位于全球模型预测的赤道附近地磁场负异常区 (EGA, 图 4a), 指示二者可能有相似的成因。对比 EGA 覆盖范围内其它地区地磁场强度结果, 发现各个地区地磁场强度在公元 1100-1400 年都有降低的趋势, 只是降低的幅度和最低值出现的时间存在差异 (图 4b-e), 指示低纬度地区核幔边界处可能普遍存在磁通量溢出现象。

由于各个地区已有数据质量和数量不一致, 目前对各地区磁异常形态特征还没有足够准确的认识。它们是同时出现还是相互之间有传递关系? 是否反映该区域核幔边界结构比较复杂? 它们在时间上是否具有周期性? 与现代地磁场的显著特征——南大西洋异常 (SAA)——有何关联? 对认识现代地磁场变化趋势有何启示? 回答上述问题, 需要更多低纬度地区不同时间的高质量数据, 同时也需要结合核幔边界结构和流体运动状态方面的相关模拟计算工作来解释其形成机制和变化规律。

参考文献

Tarduno, J.A., Watkeys, M.K., Huffman, T.N., Cottrell, R.D., Blackman, E.G., Wendt, A., Scribner, C.A., Wagner, C.L., 2015. Antiquity of the South Atlantic Anomaly and evidence for top-down control on the geodynamo. *Nat. Commun.* 6, 7865.

研究成果发表于国际著名综合期刊 *Proceedings of the National Academy of Sciences* (Cai, S., Doctor, R., Tauxe, L., Hendrickson, M., Hua, Q., Leroy, S., Phon, K., 2021. Archaeomagnetic results from Cambodia in Southeast Asia: Evidence for possible low-latitude flux expulsion. *Proceedings of the National Academy of Sciences*, 118(11), doi: 10.1073/pnas.2022490118)。本研究受国家自然科学基金委、美国国家科学基金会、中国科学院人才项目和研究所重点部署项目等资助。

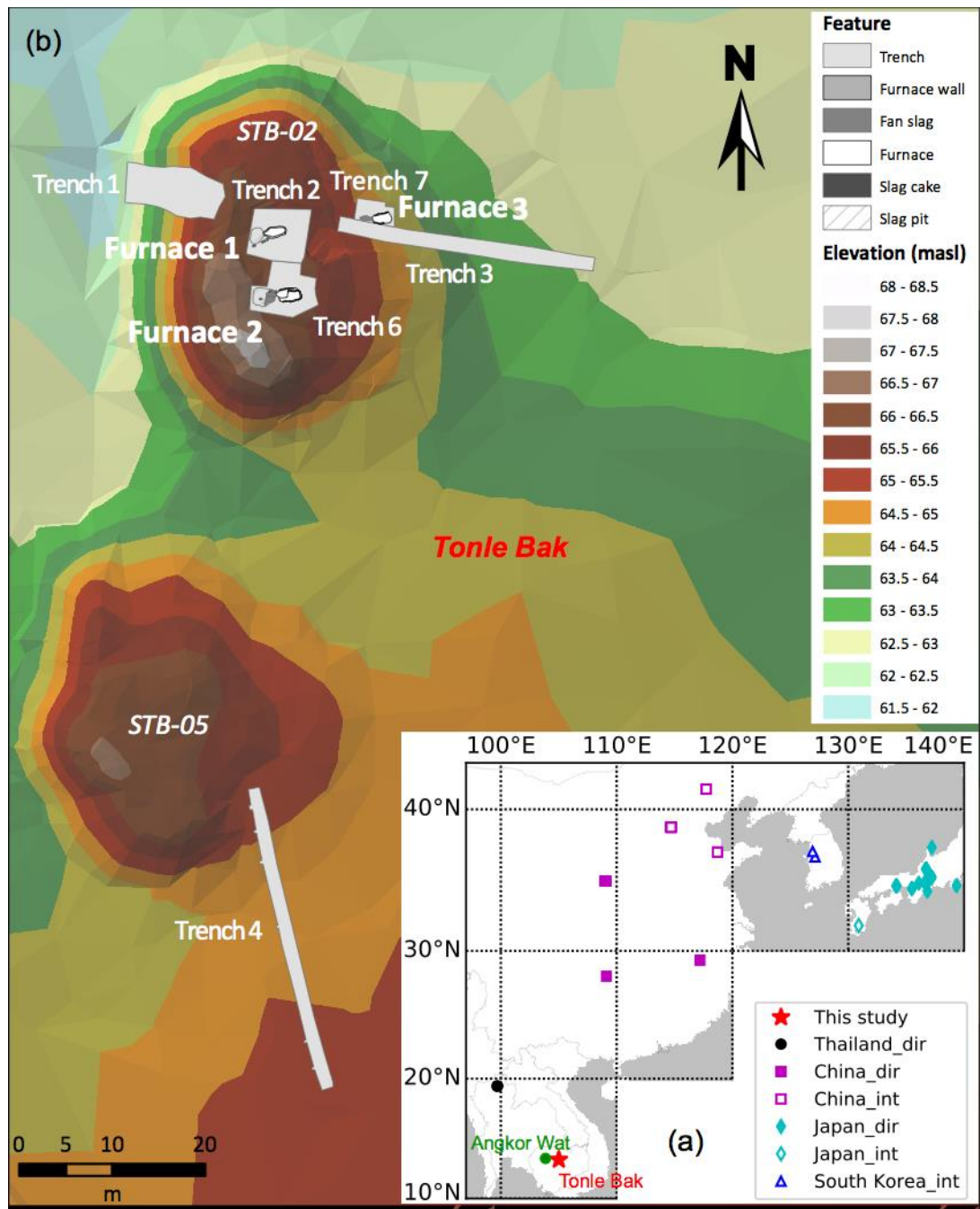


图 1. (a) 研究区位置图。红色五角星为采样位置，绿色圆形为吴哥窟位置。其余符号为本文用到的已发表数据采样位置，详见图注。(b) 采样遗址高程图。图中标明了本文采样的 3 个窑址和 3 个发掘沟位置。

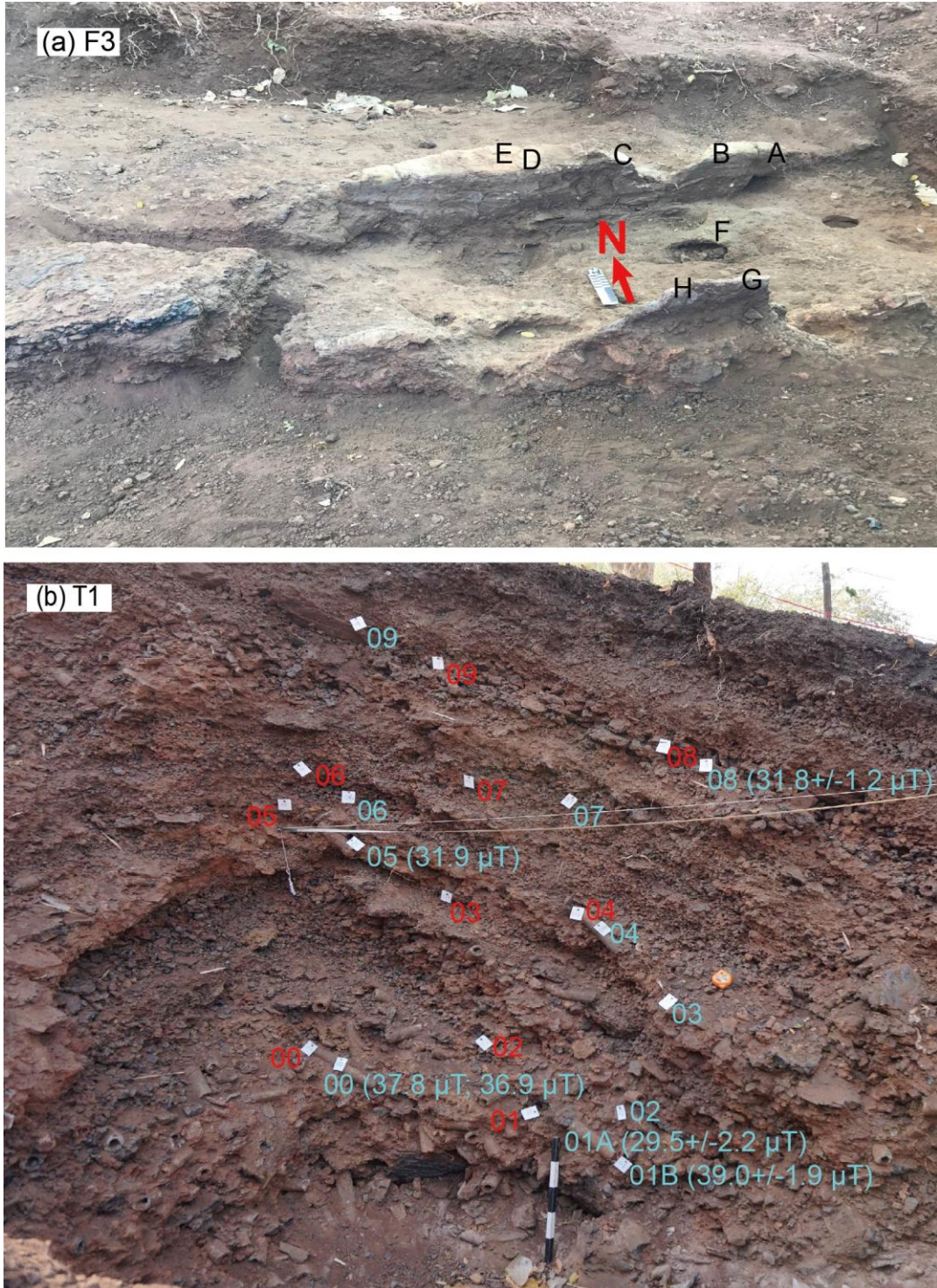


图 2. (a) 代表性窑址 (F3) 定向样品采样照片。图中字母代表定向样品采集位置。(b) 代表性发掘沟 (T1) 非定向样品和碳屑采样照片。蓝色数字为非定向样品采集位置, 旁边括号中为样品记录的古强度值, 红色数字代表碳屑采集位置。

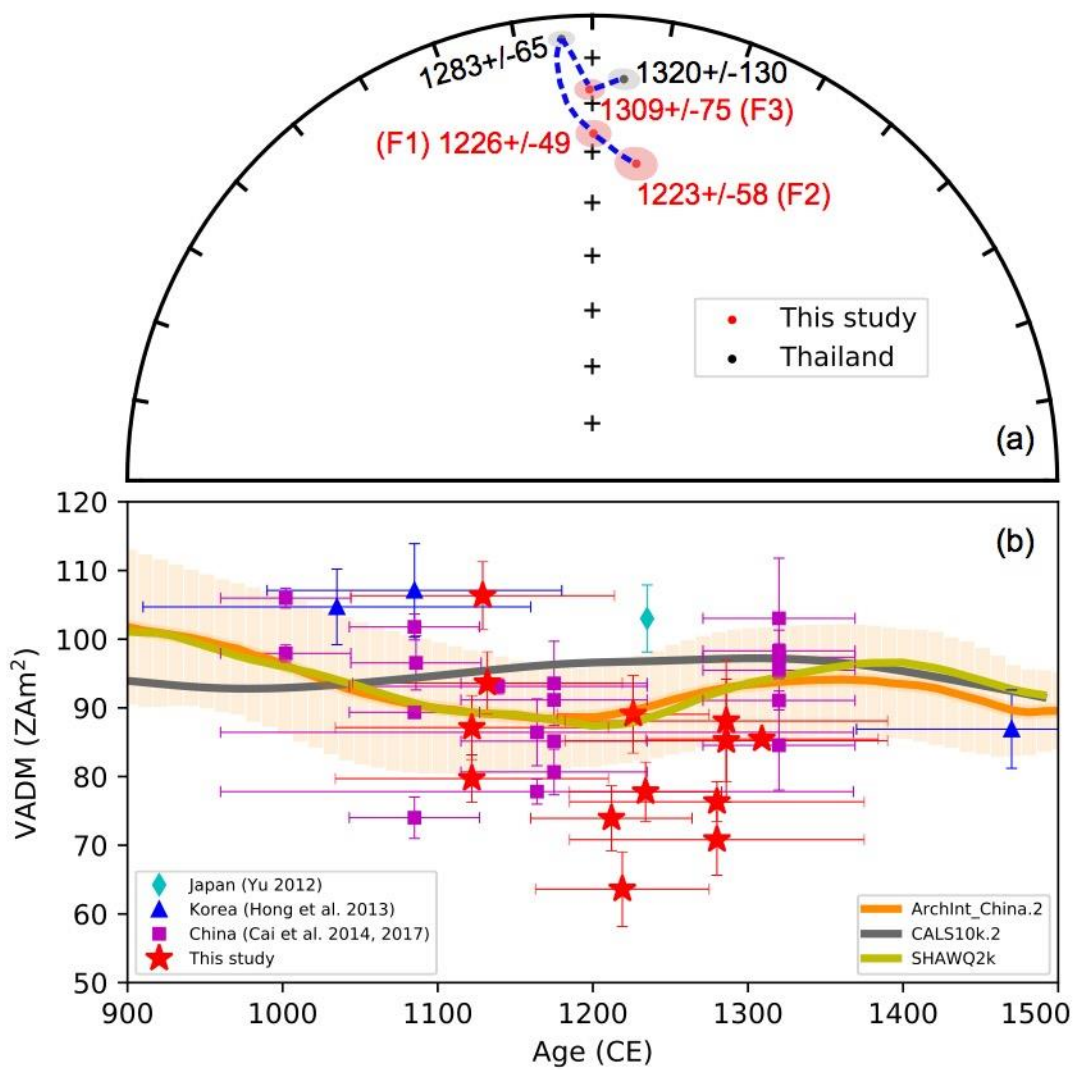


图3. (a) 地磁场方向结果。红色为本文新增结果，黑色为泰国已发表结果，蓝色虚线代表地磁场方向移动轨迹。(b) 地磁场强度结果。红色五角星为本文新增结果，其余符号为已发表数据，详见图注。桔色、灰色和黄绿色实线分别为中国考古强度参考曲线和全球模型 CALS10k.2 和 SHAWQ2k 对采样位置预测结果。

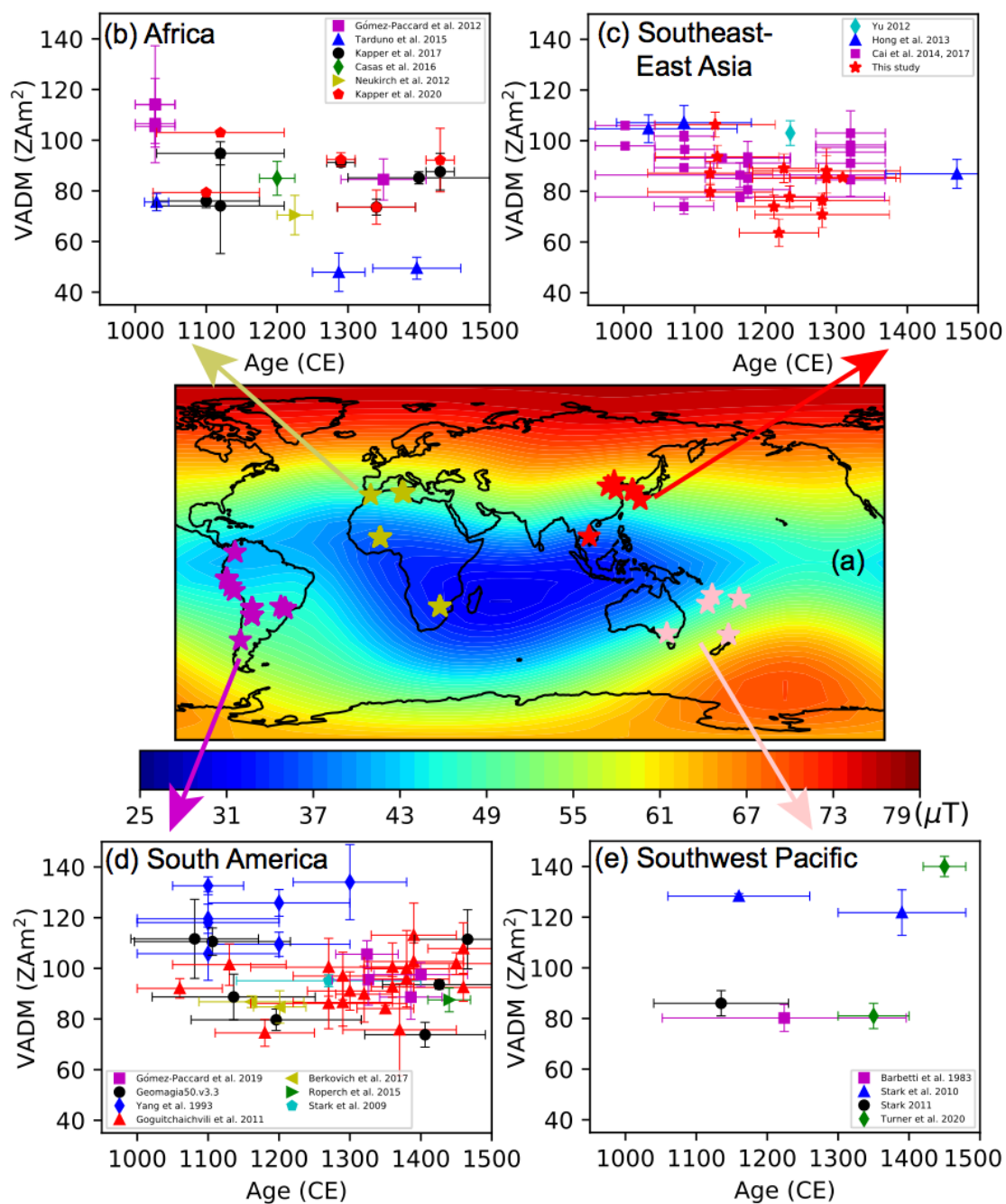


图 4. (a) 全球模型 SHAWQ2k 预测的公元 1250 年地表地磁场强度分布。(b-e) 非洲、东亚-东南亚、南美和西南太平洋地区公元 1000-1500 年地磁场强度数据，数据来源详见图注。

作者简介：



蔡书慧，博士，中国科学院地质与地球物理研究所副研究员。主要从事考古磁学及地质时期地磁场古强度研究。2014年博士毕业于中国科学院地质与地球物理研究所，2015-2018年在美国加州大学圣迭戈分校 Scripps 海洋研究所做博士后。2018年回到中国科学院地质与地球物理研究所工作。2019年获中国地球物理学会傅承义青年科技奖。2020年入选中国科学院人才计划和国家人才计划青年项目。主要成果发表在 PNAS, EPSL, GRL, JGR, GJI 等国际期刊上。

文献速递

1. 放射性核素的摇摆匹配揭示早全新世大太阳极小期在格林兰和西欧存在气候不同步震荡

翻译人：柳加波 liujb@sustech.edu.cn



Mekhaldi F, Czymzik M, Adolphi F, et al. *Radionuclide wiggle matching reveals a nonsynchronous early Holocene climate oscillation in Greenland and western Europe around a grand solar minimum*[J]. *Climate of the Past*, 2020, 16(4): 1145-1157.

<https://doi.org/10.5194/cp-16-1145-2020>

摘要：早全新世以来存在多种气候震荡，其中最知名的是前北方期震荡（Preboreal oscillation, PBO）。目前在格陵兰冰芯和欧陆记录中已经发现 PBO 和一些列的气候振荡，但是对于它们之间是如何联系尚不清楚。这主要是由于研究记录的年代存在不确定性。本文，我们提供了 BP11310—11000 年间新的高分辨率的 ^{10}Be 浓度数据。该记录来自德国具有纹泥层的 Meerfelder 玛珥湖沉积物。基于这些新数据，通过放射性核素摆动匹配，从而将该充分研究过的记录以及格陵兰冰芯记录与 IntCal13 时标进行同步。我们发现，在格陵兰岛和欧洲观察到的气候振荡在 BP 11450 和 11000 年之间是不同步的。但是，两个区域的气候震荡的结束和开始分别对应着大太阳极小期的开始。在一系列的北大西洋区域气候的太阳驱动模拟研究中，也发现了类似的地球空间异常。我们进一步推测，北大西洋的淡水输送可能会放大太阳驱动力，这是由于大西洋经向翻转环流（AMOC）的减弱能够增强该地区的地表气温异常。

ABSTRACT: Several climate oscillations have been reported from the early Holocene superepoch, the best known of which is the Preboreal oscillation (PBO). It is still unclear how the PBO and the number of climate oscillations observed in Greenland ice cores and European terrestrial records are related to one another. This is mainly due to uncertainties in the chronologies of the records. Here, we present new, high-resolution ^{10}Be concentration data from the varved Meerfelder Maar sediment

record in Germany, spanning the period 11 310–11 000 years BP. These new data allow us to synchronize this well-studied record, as well as Greenland ice core records, with the IntCal13 timescale via radionuclide wiggle matching. In doing so, we show that the climate oscillations identified in Greenland and Europe between 11 450 and 11 000 years BP were not synchronous but terminated and began, respectively, with the onset of a grand solar minimum. A similar spatial anomaly pattern is found in a number of modeling studies on solar forcing of climate in the North Atlantic region. We further postulate that freshwater delivery to the North Atlantic would have had the potential to amplify solar forcing through a slowdown of the Atlantic meridional overturning circulation (AMOC) reinforcing surface air temperature anomalies in the region.

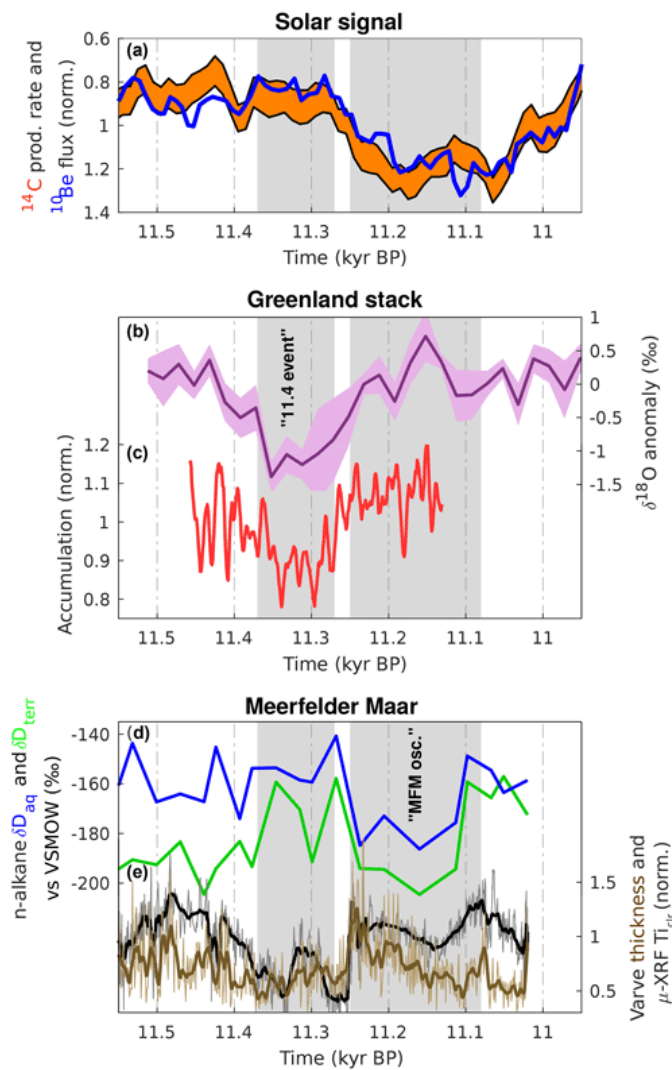


Figure 1: (a) ^{14}C production rate (orange envelope) and GRIP ^{10}Be data (blue) on a reversed y axis to indicate variations in solar activity. (b) The $\delta^{18}\text{O}$ stack from the DYE-3, GRIP, NGRIP, and Renland ice

cores (Rasmussen et al., 2007; Vinther et al., 2009) is shown in magenta, and (c) the modeled accumulation anomalies from Rasmussen et al. (2007) for DYE-3, GRIP, and NGRIP are shown in red. (d) The δD data record from lipid biomarkers of MFM sediments (Rach et al., 2014) is plotted in blue and green (aquatic and terrestrial), while (e) varve thickness (Martin-Puertas et al., 2012a) and varve μ -XRF Tielr (Martin-Puertas et al., 2017) are plotted in brown and black, respectively. The gray bands depict the time of occurrence of the 11.4 ka event in Greenland and of the cold oscillation inferred from the MFM sediments (MFM oscillation). All data are plotted on the IntCal13 timescale as per Figure. 2.

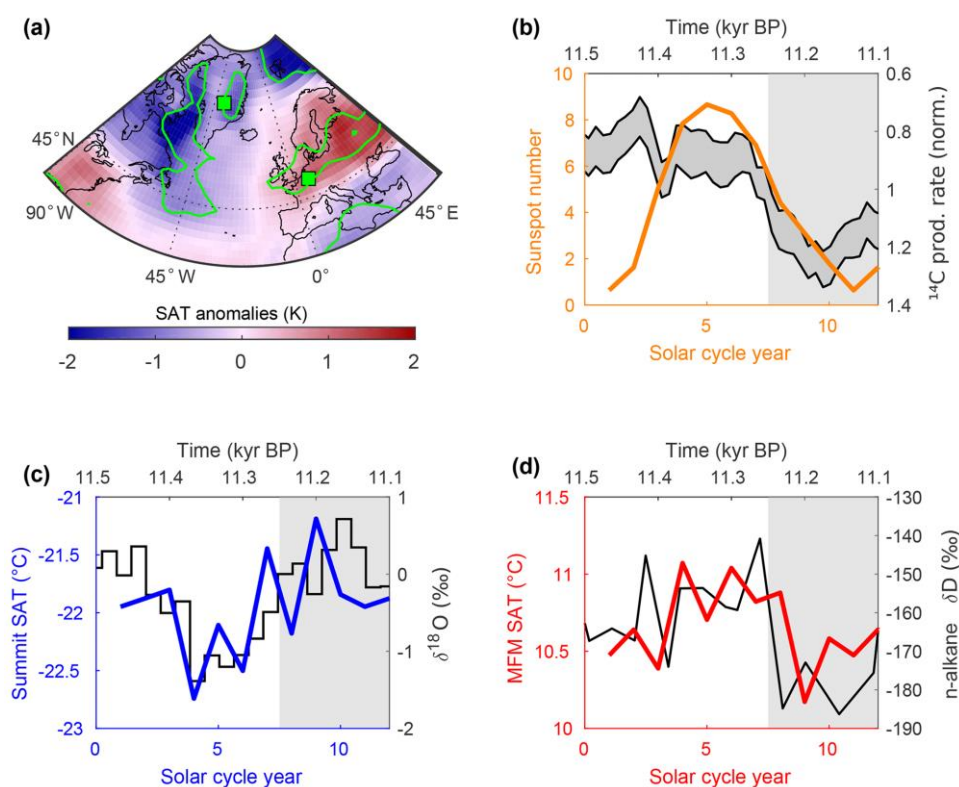


Figure 2: The 11.4 ka event and MFM oscillation compared to the solar forcing of 20th century SATs in the North Atlantic region as seen in 20CR. (a) Surface air temperature (SAT) anomalies for solar maximum winters (DJF) compared to solar minimum winters (see Figure. S2) for the period 1946–2011 CE in 20th century climate reanalysis (Compo et al., 2011). The green squares point to the location of Summit and of MFM, while the green contour lines represent significance levels for $p < 0.1$ (t test). Years influenced by large tropical volcanic eruptions have been removed as per Ineson et al. (2011). (b) The transition between high to low solar activity in the ^{14}C production rate data (gray envelope, top and right axes) compared to the mean sunspot group number of all 11-year solar cycles between 1900 and 2011 CE (orange curve, bottom and left axes). (c) The $\delta^{18}\text{O}$ stack (black curve, top and right axes) shown

in Figure. 3b compared to the mean SAT at Summit (blue curve, bottom and left axes) throughout all 11-year solar cycles between 1900 and 2011 CE as in (b). (d) Same as (c) but with δD (black curve, top and right axes) and MFM SAT (red curve, bottom and left axes). Note the different timescale on the top (paleoclimate records) and bottom (reanalysis data) axes. The gray bands show the periods of low solar activity occurring in the two time periods that are compared.

2. 西太平洋副热带高压与亚洲夏季风并置形成了亚热带东亚降水



翻译人：仲义 zhongyi@sustech.edu.cn

Xu, H., Goldsmith, Y., Lan, J.H., et al., Justaposition of Western Pacific Subtropical High on Asian Summer Monsoon Shapes Subtropical East Asian Precipitation [J] Geophysical Research Letters, 2020, 47(3), e2019GL084705.

<https://doi.org/10.1029/2019GL084705>

摘要：越来越多的证据质疑亚洲夏季风的均一性响应（ASM）降水模式，因此，我们需要重新思考其控制机制。本文通过展示亚热带澄海湖 15000 年的定量降水历史，结果显示湖水位和沉降量在 Bolling-Allerod、全新世早期和晚期较高，而在全新世中期处于低值。轨道尺度上降水趋势与北方夏季日射量不一致性，普遍认为北方夏季日射量是夏季降水的驱动因素。澄海湖长期湖水位与热带太平洋海面温度趋势、相关的区域性海表温度梯度以及半球间的温度梯度是同步变化的。作者认为半球间和纬向太平洋温度梯度的变化调节了西太平洋副热带高压的强度和位置，从而导致了东亚副热带水文气候的异质性。

ABSTRACT: Increasing lines of evidence question the homogenous response of Asian Summer Monsoon (ASM) precipitation patterns, requiring rethinking of the forcing mechanisms. Here we show a ~15,000 - year quantitative precipitation history based on well - dated lake levels at Lake Chenghai, subtropical China. Lake levels and the inferred precipitation were high during the Bølling - Allerød, early and late Holocene, but low during the middle Holocene. The orbital scale precipitation trend is out of phase with boreal summer insolation, the later has been widely suggested as the driver of ASM precipitation. Lake Chenghai long-term lake levels are synchronous with trends in tropical Pacific sea surface temperatures, the related zonal sea surface temperature gradients, and interhemispheric temperature gradients. We propose that changes in either the interhemispheric or zonal Pacific temperature gradients modulate the intensity and location of the western Pacific subtropical high, which is juxtaposed on the ASM, leading to heterogeneous

hydroclimatic conditions over subtropical East Asia.

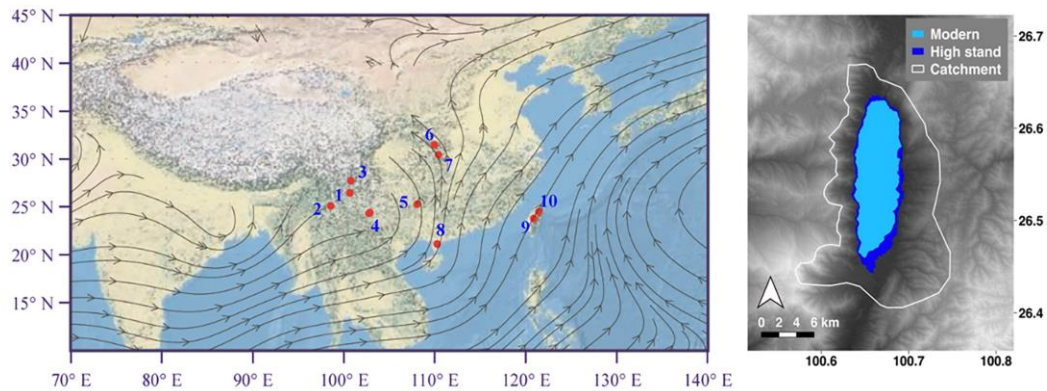


Figure 1. (left) Location of Lake Chenghai and the sites mentioned in the text (see below). The gray arrows show streamlines (at 850 hPa) averaged between June to August of 1968–1996 based on National Centers for Environmental Prediction/National Center for Atmospheric Research reanalysis data (Kalnay et al., 1996). (right) A digital elevation model image of Lake Chenghai with modern and high lake stands, and catchment boundary. The numbers in the left panel denote parts of the sites mentioned in the text: (1) Lake Chenghai (this study), (2) Qinghai Lake in Tengchong County (E. L. Zhang et al., 2017), (3) Lake Lugu (E. L. Zhang et al., 2018), (4) Lake Xingyun and Lake Fuxian (Li et al., 2019; Wu et al., 2018), (5) Dongge Cave (Dykoski et al., 2005), (6) Dajiuhu peatland (Xie et al., 2013), (7) Heshang Cave (Zhu et al., 2017), (8) Lake Huguangyan (HGY; Yancheva et al., 2007), (9) Toushe peat bog (Liew et al., 2006), and (10) Retreat Lake (Selvaraj et al., 2007).

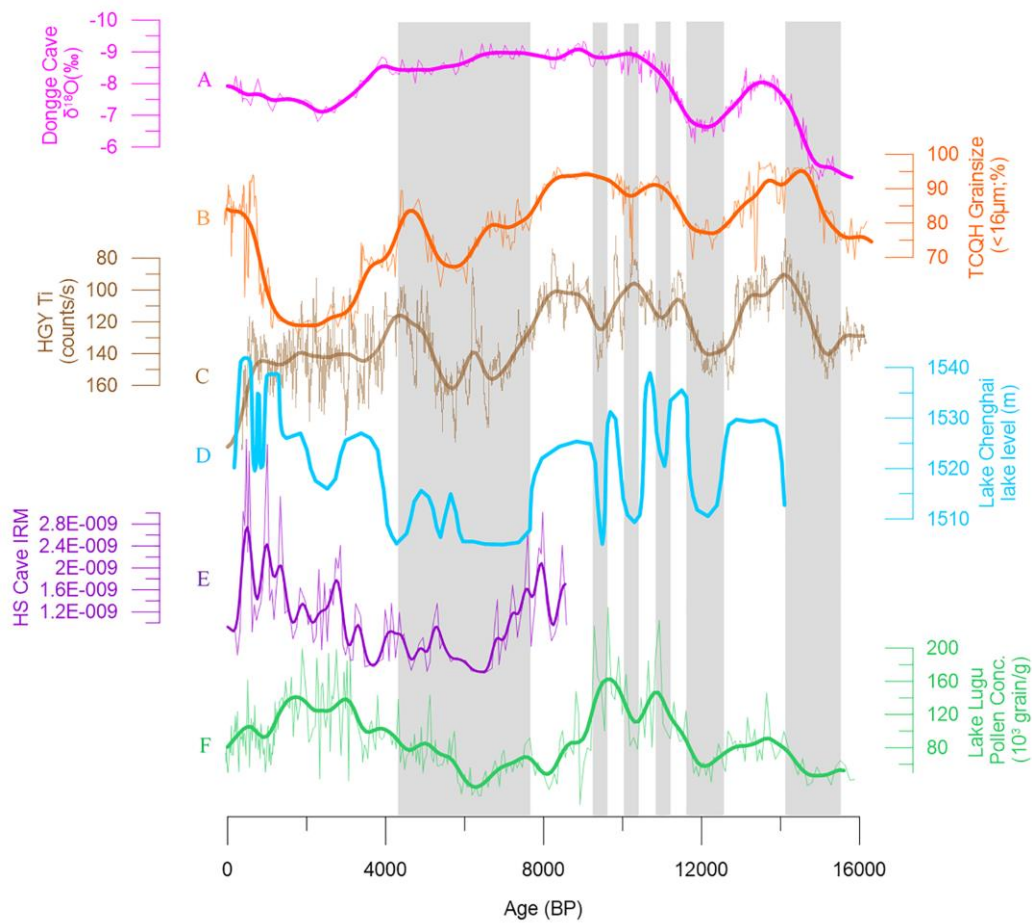


Figure 2. Comparison between Lake Chenghai lake level (curve D; blue thick; this study) and other Asian monsoon proxy indices. (a) Dongge Cave $\delta^{18}\text{O}$ curve (pink; Dykoski et al., 2005). (b) Sedimentary grainsize (orange) from Tengchong Qinghai Lake (TCQH; E. L. Zhang et al., 2017). (c) Sedimentary Ti contents (brown) from Lake Huguangyan (Yancheva et al., 2007). (e) Isothermal Remanent Magnetization (IRM) index (purple) from Heshang Cave (Zhu et al., 2017). (f) Pollen concentration (green) from Lake Lugu (E. L. Zhang et al., 2018). The vertical gray columns show broadly synchronous monsoon weakenings between different records from Bølling - Allerød to mid-Holocene.

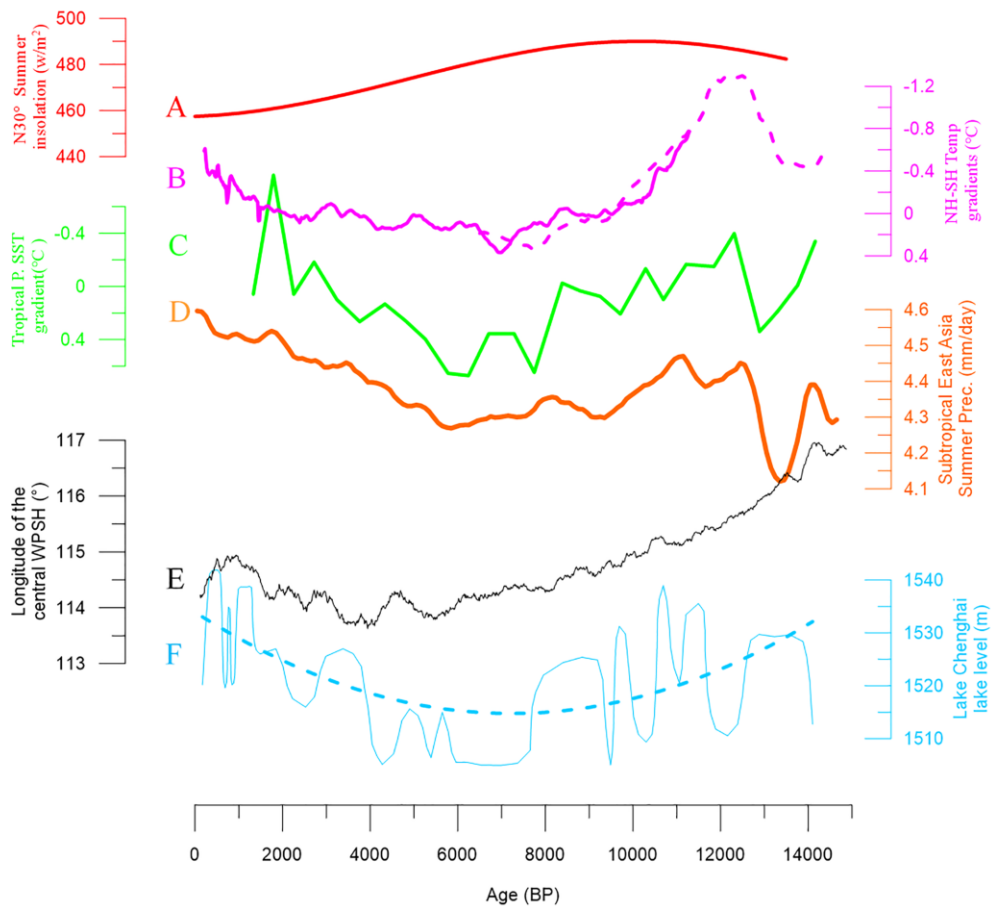


Figure 3. Potential drivers of the long - term subtropical East Asia precipitation. (a) Summer insolation at 30°N (red; Berger, 1978). (b) North - south hemisphere temperature gradients (the pink line is from McGee et al., 2014, and the pink dotted line is from Shakun et al., 2012). (c) Normalized tropical pacific sea surface temperature gradient (green; Koutavas & Joanides, 2012). (d) Simulated summer (June - July - August) precipitation (20–27°N,110–125°E) extracted from TraCE - 21ka simulation (orange; Liu et al., 2014). (e) Longitude of the central western Pacific subtropical high (WPSH; black) based on TraCE - 21ka simulation (Liu et al., 2014). (f) LC lake levels (blue, this study; the blue - dotted line is the two-order polynomial fit).

3. 自生胶黄铁矿指示新西兰 Hikurangi 边缘含天然气水合物的沉积物中甲烷扩散



翻译人:李园洁 liyj3@sustech.edu.cn

Kars M, Greve A, Zerbst L. *Authigenic Greigite as an Indicator of Methane Diffusion in Gas Hydrate-Bearing Sediments of the Hikurangi Margin, New Zealand*[J]. *Frontiers in Earth Science*, 2021, 9: 80.

<https://doi.org/10.3389/feart.2021.603363>

摘要: 自生亚铁磁性铁硫化物, 尤其是胶黄铁矿(Fe_3S_4) 广泛存在活动增生楔的含天然气水合物的海洋沉积物中。胶黄铁矿是微生物活动的产物, 因而可以指示与天然气水合物密切相关的微生物过程。本文, 作者对大洋航次 375 的 U1518 钻孔的岩芯进行了高分辨的岩石磁学实验, 该孔位于新西兰近海 Hikurangi 边缘的增生楔上。样品主要为从海底到深 492m (包括 Pāpaku 破碎带) 的沉积序列。本次研究的主要目的是获得 U1518 岩芯的岩石磁学性质和磁性矿物成分。根据随着深度磁性矫顽力的变化, 沉积序列可以分为 5 个连续区域, 大部分样品具有高矫顽力, 一阶反转曲线 (FORC) 图为典型的单畴胶黄铁矿。断层上行的顶部表现出低矫顽力与破碎带和下行更低的矫顽力类似。U1518 广泛分布的胶黄铁矿与甲烷扩散和主要分布在沉积物中的甲烷水合物相关。在三个上行天然气富集层, 表现出更强的 FORC 信号, 可能与微生物活动增强有关, 有助于胶黄铁矿的形成和保存。我们在 Hikurangi 边缘的发现表明, 胶黄铁矿, 甲烷和微生物活动之间密切联系。

ABSTRACT: Authigenic ferrimagnetic iron sulfides, essentially greigite (Fe_3S_4), are commonly found in gas hydrate-bearing marine sediments of active accretionary prisms. Greigite is a by-product, either intracellular or extracellular, of microbial activity, and therefore provides good indication of microbial processes which are closely related to the occurrence of gas hydrate. A high-resolution rock magnetic study was conducted at Site U1518 of International Ocean Discovery Program Expedition 375, located in the frontal accretionary wedge of the Hikurangi Margin, offshore New Zealand. Samples were collected throughout the entire recovered stratigraphic

sequence, from the surface to ~492 m below seafloor (mbsf) which includes the Pā-paku fault zone. This study aims to document the rock magnetic properties and the composition of the magnetic mineral assemblage at Site U1518. Based on downhole magnetic coercivity variations, the studied interval is divided into five consecutive zones. Most of the samples have high remanent coercivity (above 50 mT) and first-order reversal curves (FORC) diagrams typical of single-domain greigite. The top of the hanging wall has intervals that display a lower remanent coercivity, similar to lower coercivities measured on samples from the fault zone and footwall. The widespread distribution of greigite at Site U1518 is linked to methane diffusion and methane hydrate which is mainly disseminated within sediments. In three footwall gas hydrate-bearing intervals, investigated at higher resolution, an improved magnetic signal, especially a stronger FORC signature, is likely related to enhanced microbial activity which favors the formation and preservation of greigite. Our findings at the Hikurangi Margin show a close linkage between greigite, methane hydrate and microbial activity.

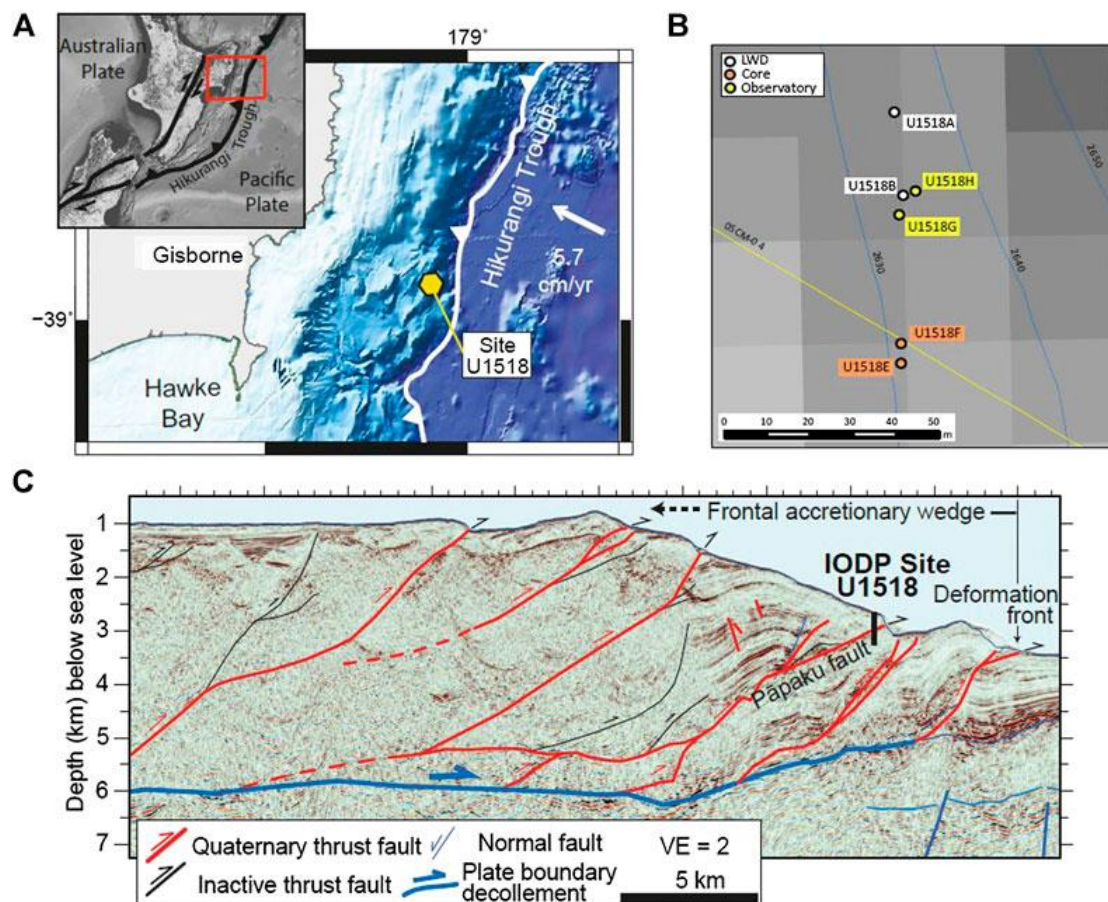


Figure 1. (A) Location and geotectonic setting of the Hikurangi subduction margin and the New Zealand plate boundary (inset). Displayed in the bathymetric map of the northern Hikurangi subduction margin

are also the main thrust faults, IODP Site U1518 and the relative plate convergence vector (B) Detailed locationmap of holes drilled at Site U1518 (from Saffer et al., 2019) (C) Seismic cross section of the frontal accretionary wedge near the drilling transect of IODP Expedition 375, including interpretation after Barker et al. (2018). The location of IODP Site U1518 and trace of the Papaku fault are indicated. Figures (A) and (C) are modified from Fagereng et al. (2019) and Greve et al. (2020).

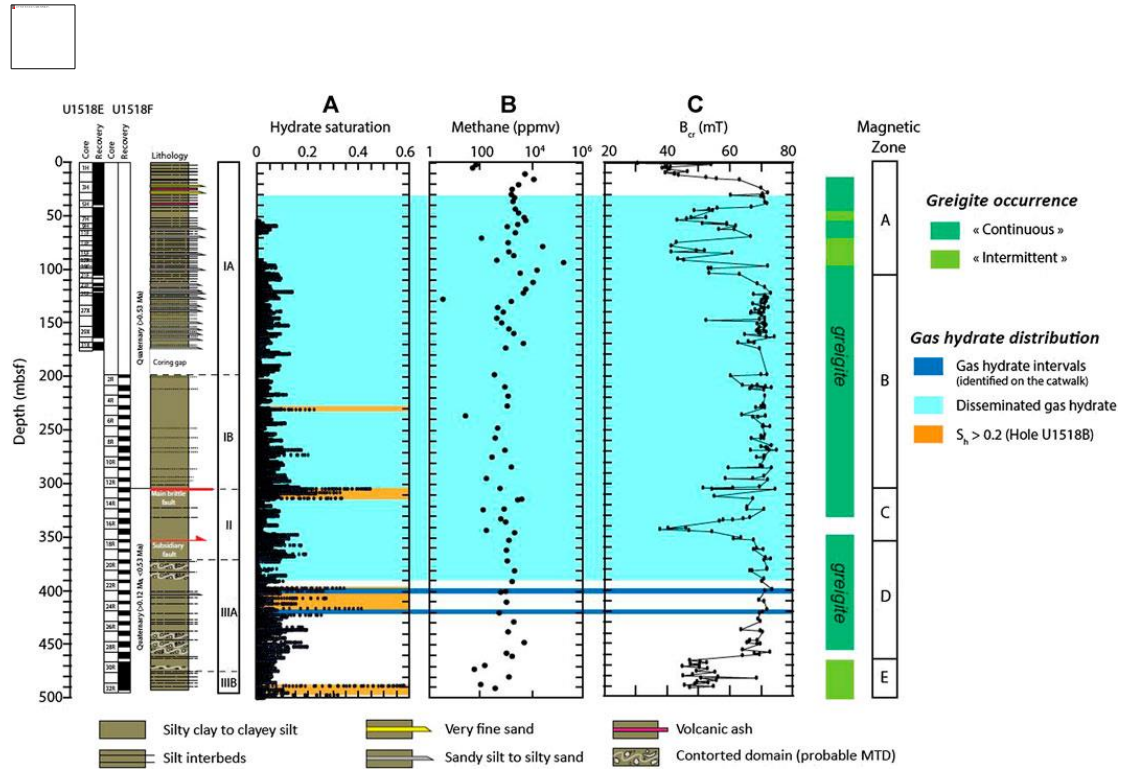


Figure 2. Distribution of gas hydrate at Site U1518 based on shipboard observations (Wallace et al., 2019) (A) Hydrate saturation calculated from LWD resistivity data (Cook et al., 2020). Here a value of $n = 2.5$ for hydrate saturation calculation with Archie’s equation has been used (Cook and Waite, 2018) (B) Shipboard methane contents (C) Remanent coercivity B_{cr}. Occurrence of greigite (dark green: continuous, light green: intermittent) from rock magnetic measurements is reported on the right with the coercivity zones defined in this study. The light blue shaded zone corresponds to disseminated gas hydrate and the dark blue shaded zones correspond to three gas hydrate-bearing sections identified aboard on the catwalk. The orange shaded zones correspond to intervals in Hole U1518B where hydrate saturation S_h calculated from LWD resistivity data exceeds 0.2 (Cook et al., 2020). Core recovery, age and lithologic description are from Wallace et al. (2019).

4. 来自伊豆-小笠原-马里亚纳弧发育早期的高度难熔地幔源区的玄武岩



翻译人：冯婉仪 fengwy@sustech.edu.cn

Li H, Arculus R J, Ishizuka O, et al. *Basalt derived from highly refractory mantle sources during early Izu-Bonin-Mariana arc development* [J]. *Nature communications*, 2021, 12: 1723.

<https://doi.org/10.1038/s41467-021-21980-0>

摘要：俯冲带和弧发育早期的岩浆特征不同于成熟体系。早期的伊豆-小笠原-马里亚纳（IBM）体系以低钛-钾拉斑玄武岩和玻安岩为主。从位于 IBM 最古老残余弧西部的 Amami Sankaku 盆地（ASB）获取的玄武岩的喷发时间约为 49 Ma。这是以弧前玄武岩（FAB）为代表的俯冲开始（51-52 Ma）之后的 3 Ma，处于 FAB-boninite 与典型的弧岩浆活动之间的转折点。研究表明，ASB 玄武岩为低钛-钾、含铝尖晶石的拉斑玄武岩，与大洋中脊（MOR）、弧后盆地、岛弧或洋岛的玄武岩明显不同。它们的上地幔源区是热的、还原的、难熔的橄榄岩，表明之前已经发生过熔体提取。ASB 玄武岩从斜长石-尖晶石橄榄岩相边界处（压力约为 0.7-2 GPa）迅速喷发至地表。不同压力-不同温度的矿物痕迹被保存在该玄武岩中，并没有在典型的 MOR 或成熟弧的持续补给-混合-排出-分馏阶段被抹掉。

ABSTRACT: The magmatic character of early subduction zone and arc development is unlike mature systems. Low-Ti-K tholeiitic basalts and boninites dominate the early Izu-Bonin-Mariana (IBM) system. Basalts recovered from the Amami Sankaku Basin (ASB), underlying and located west of the IBM's oldest remnant arc, erupted at ~ 49 Ma. This was 3 million years after subduction inception (51-52 Ma) represented by forearc basalt (FAB), at the tipping point between FAB-boninite and typical arc magmatism. We show ASB basalts are low-Ti-K, aluminous spinel-bearing tholeiites, distinct compared to mid-ocean ridge (MOR), backarc basin, island arc or ocean island basalts. Their upper mantle source was hot, reduced, refractory peridotite, indicating prior melt extraction. ASB basalts transferred rapidly from pressures (~ 0.7-2 GPa) at the plagioclase-spinel peridotite facies boundary to the surface. Vestiges of a polybaric-polythermal mineralogy are preserved in this basalt, and were not obliterated during

persistent recharge-mix-tap-fractionate regimes typical of MOR or mature arcs.

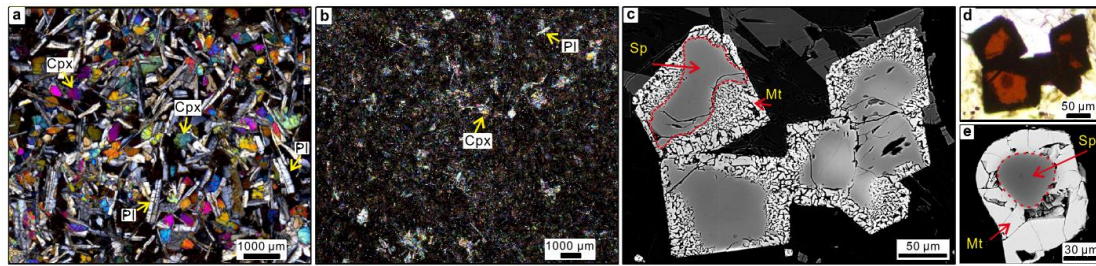


Figure 1. General and detailed photomicrographs of Unit 1 ASB basalts. a Medium-grained basalt from subunit 1c (78R3 21–25), including clinopyroxene (Cpx) and plagioclase (Pl) crystals (crossed polars). b Fine-grained basalt (84R1 84–87) from subunit 1e, with small crystals of clinopyroxene and plagioclase (crossed polars). c Back-scatter electron images of spinel; darker colour within the red dash line is aluminous spinel (Sp); brighter colour outside the red dash line is symplectitic magnetite (Mt). d Transmitted light image of the same spinel shown in c, red colour is the Al-rich cores, and opaque boundaries are magnetite. e Back-scatter image of spinel, Al-rich core surrounded by magnetite-rich rim outside the red dash line.

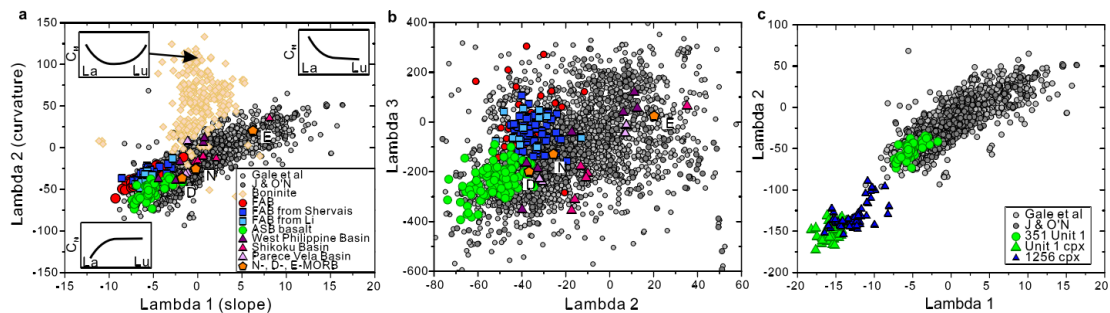


Figure 2. Shape coefficients of rare earth element patterns⁵³ for comparison of Unit 1 ASB basalts with FAB, MORB/G, and backarc basin basalts of the Philippine Sea Plate. Data sources for a and b are Unit 126, MORB from Gale et al.²⁸ and Jenner & O'Neill⁵⁶, boninite^{20,67,68}, FAB of Izu-Bonin-Mariana^{11,54,55} and literature cited in ref. 19. a Lambda 2 (curvature) versus lambda 1 (slope). Schematic chondrite-normalised REE abundance patterns characterised variously by light REE-depletion, enrichment and U-shaped patterns of boninite are shown in the corners of this plot. N-, D-, E-MORB represent normal MORB, depleted MORB, and enriched MORB. b Lambda 3 (sigmoidal character) versus lambda 2. c Lambda 2 versus lambda 1 comparing clinopyroxene from Unit 1 and gabbros at Site 125669 with ocean floor basalts^{28,56} and Unit 1 bulk rock²⁶.

5. 东亚下方的水平板片及其柔和的动力学响应



翻译人：刘伟 inewway@163.com

Liu Shaofeng, Ma Pengfei, Zhang Bo, et al. *The Horizontal Slab Beneath East Asia and Its Subdued Surface Dynamic Response [J]. JGR-Solid Earth, 2021.*

<https://doi.org/10.1029/2020JB021156>

摘要：板块构造运动、变形和动力地形响应于板块与地幔耦合。东亚的构造特征是在地幔转换带内存在一个异常巨大的水平板片。这一构造特征是如何演变的，以及如何与板块构造运动、变形和地形相联系的，还知之甚少。基于地震层析成像推断的地幔结构，我们展示了四维地球动力学重建的结果。研究发现，中新世期间，俯冲的西太平洋板块被顺时针旋转的菲律宾海板块逐渐撕裂，俯冲过程中，西北方向的地幔流动促进了水平板片的形成，导致东亚边缘的动态沉降。在没有大规模海洋淹没或板块回退的时期内，动态地形的相当微弱的变化与残余地形的变化一致，仅在过去 50 Myr 变化 200 m 左右。东亚的构造和地形与东南亚形成了强烈的对比，反映了板片短暂地停滞在东亚下面的地幔中，同时崩塌进入东南亚下面的下地幔中。

ABSTRACT: The kinematics of plate tectonics, deformation, and dynamic topography are strong indicators of coupling between plates and the mantle. East Asia is characterized by the presence of an unusually large horizontal slab that lies within the mantle transition zone. How this feature evolved and is linked to plate tectonics, deformation, and topography is poorly understood. Here, we show four - dimensional geodynamic modeling results constrained by a new deforming plate reconstruction that fits mantle architecture inferred from seismic tomography. We find that the subducted western Pacific slab was progressively torn by the Philippine Sea plate rotating clockwise during the Miocene and that northwestward mantle flow contributed to shaping the horizontal slab during subduction, leading to dynamic subsidence along the East Asia margin. The rather subdued change in dynamic topography, predicted from those models that fit the horizontal slab in the mantle, is consistent with the variation in residual topography, recorded in the stratigraphy, within only about

± 200 m over the last 50 Myr during a period of no large marine inundation or retreat. The tectonics and topography of East Asia strongly contrast with those of Southeast Asia and are reflective of slabs ephemerally stagnating in the mantle below East Asia while avalanching into the lower mantle below Southeast Asia.

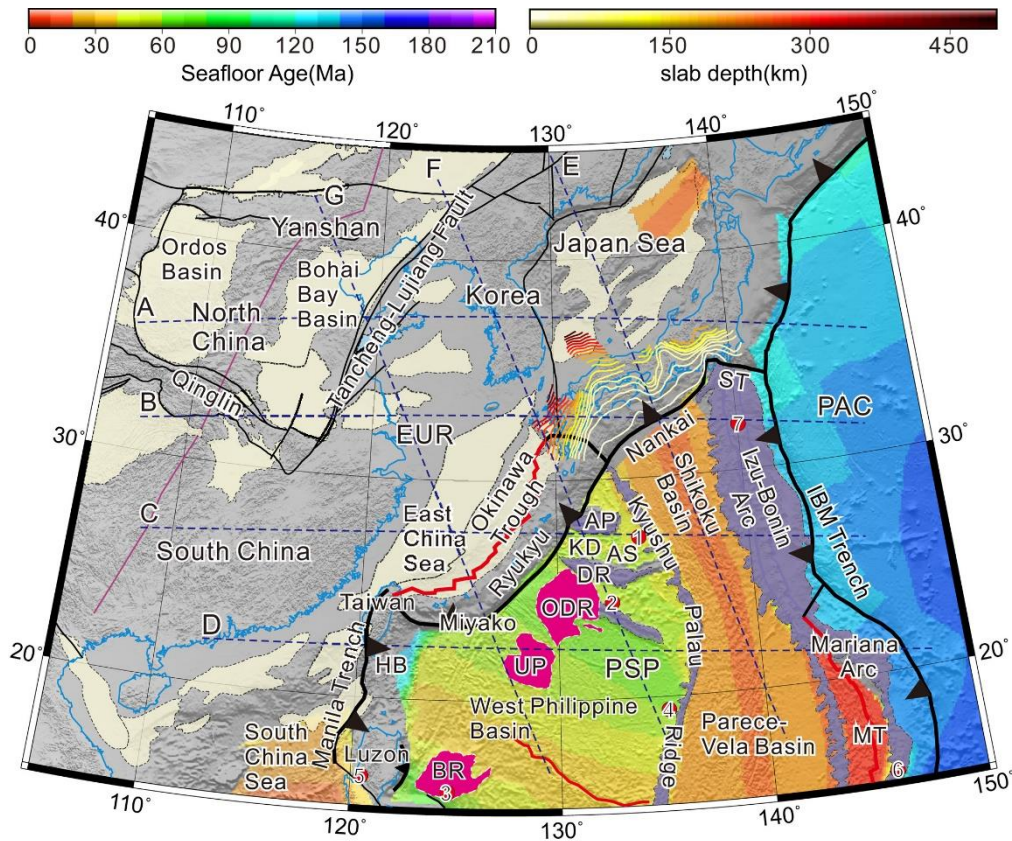


Figure 1. East Asia tectonic map. The morphology of the Philippine Sea slab beneath SW Japan is shown by contours colored by depth. Basins are depicted as light - yellow regions. Regional faults in ocean and continent and seafloor spreading centers are shown as thick and thin black lines and thick red lines, respectively. Sky - blue lines represent present day coastlines. The locations of regional selected profiles (a) - (g) are indicated by the blue dashed lines. Arcs and relic arcs and ocean island basalt in the Philippine Sea plate are depicted as blue - purple areas and magenta polygons, respectively. The pink line represents the gravity gradient zone (Zheng et al., 2006). Drilling and paleomagnetic sampling sites: 1 = IODP Site U1438; 2 = DSDP 446; 3 = ODP 1201; 4 = Luzon; 5 = DSDP 292; 6 = Saipan; 7 = Izu - Bonin. EUR = Eurasian Plate; PSP = Philippine Sea Plate; PAC = Pacific plate; IBM = Izu - Bonin - Mariana Trench; ST = Sagami Trough; HB = Huatung basin; AS = Amami - Sankaku basin; KD = Kita - Daito basin; AP = Amami Plateau; DR = Daito Ridge; ODR = Oki - Daito Rise; UP = Urdaneta Plateau; BR = Benham Rise.

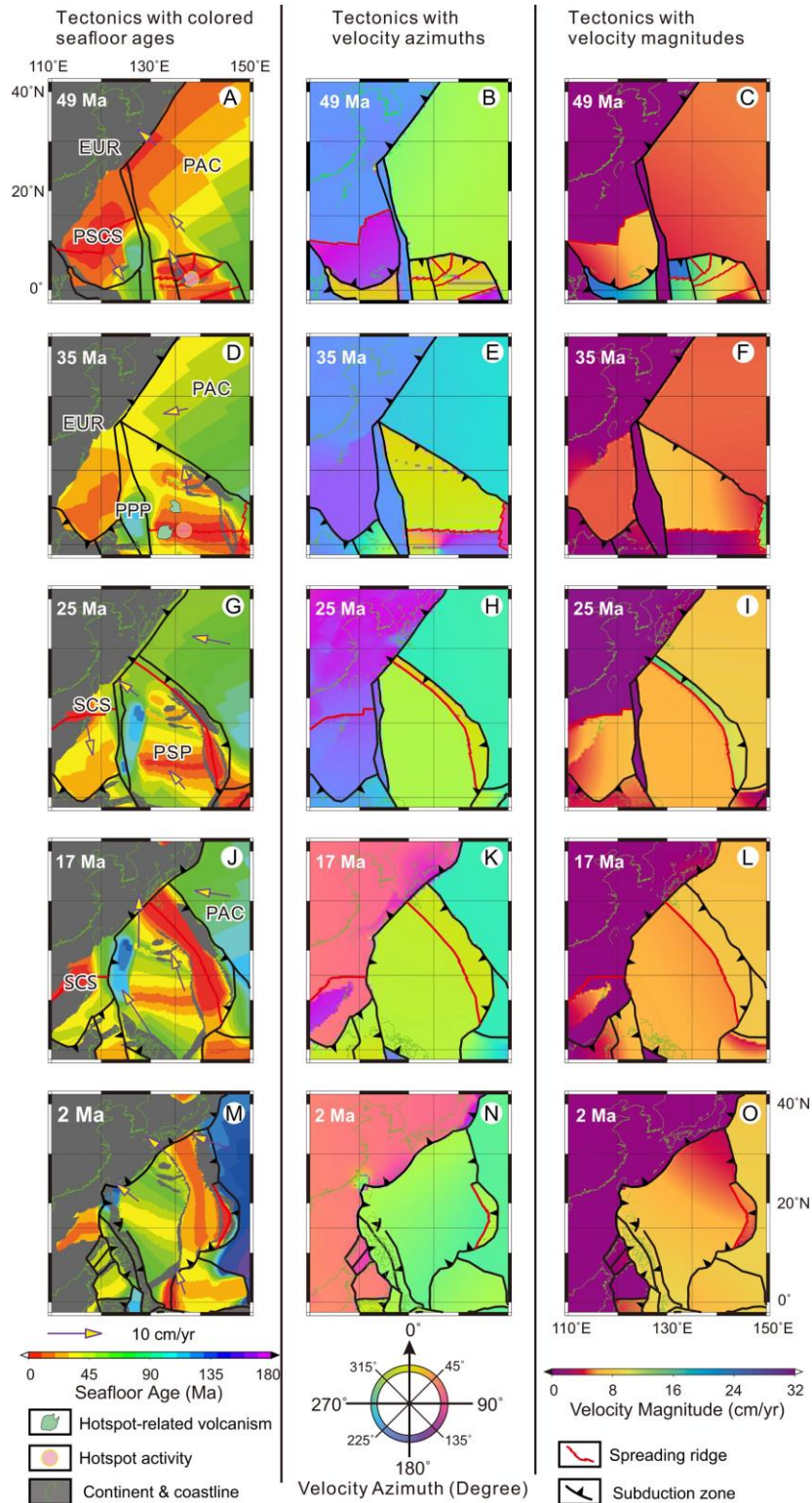


Figure 2. Reconstructed tectonic and coupled plate motion history of East Asia at 49, 35, 25, 17, 10, and 2 Ma in the absolute reference system. The subFigures in the left column show the tectonics with colored seafloor ages, and the subFigures in the middle and right columns show the corresponding velocity

azimuths and magnitudes over the region, respectively. PPP = proto - Philippine Sea plate, PSCS = proto - South China Sea. The other symbols are the same as those in Figure 1.

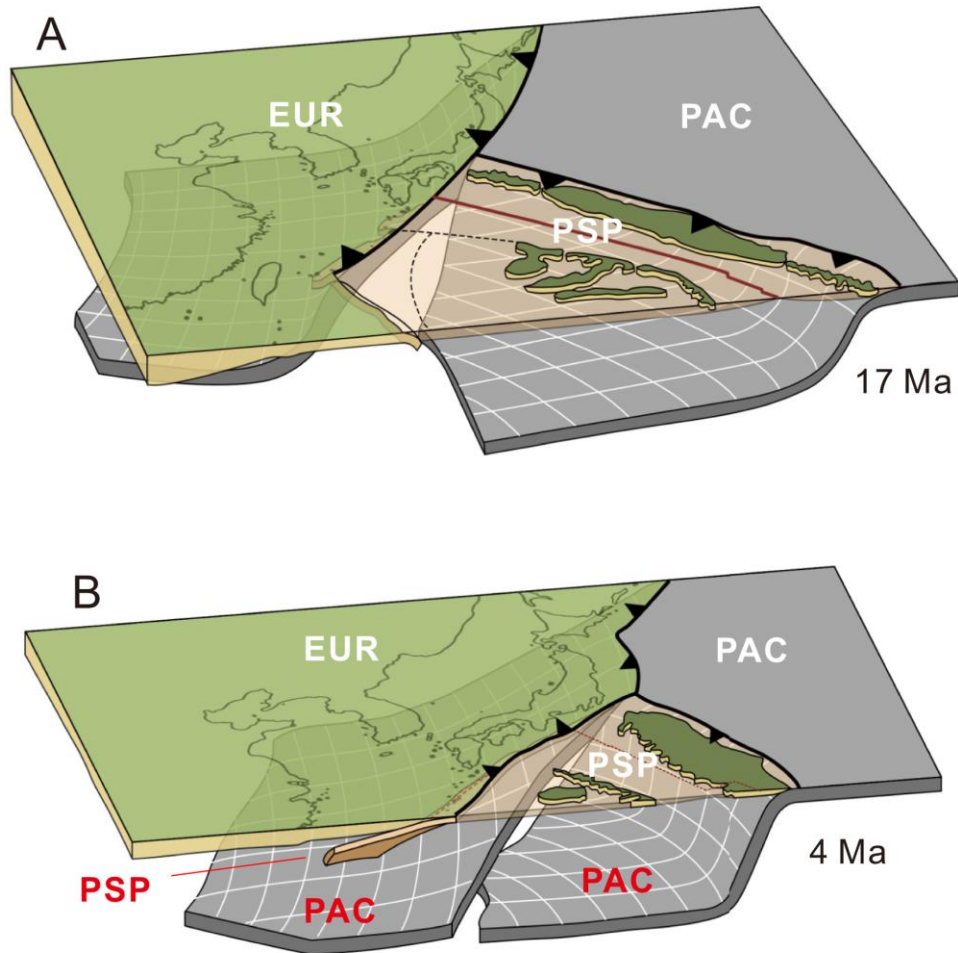


Figure 3. Stereograph exhibiting the geodynamic process associated with triple junction migration and Pacific slab tearing along the East Asian margin at ~17 Ma (a) and 4 Ma (b). The other symbols are the same as those in Figure 1.

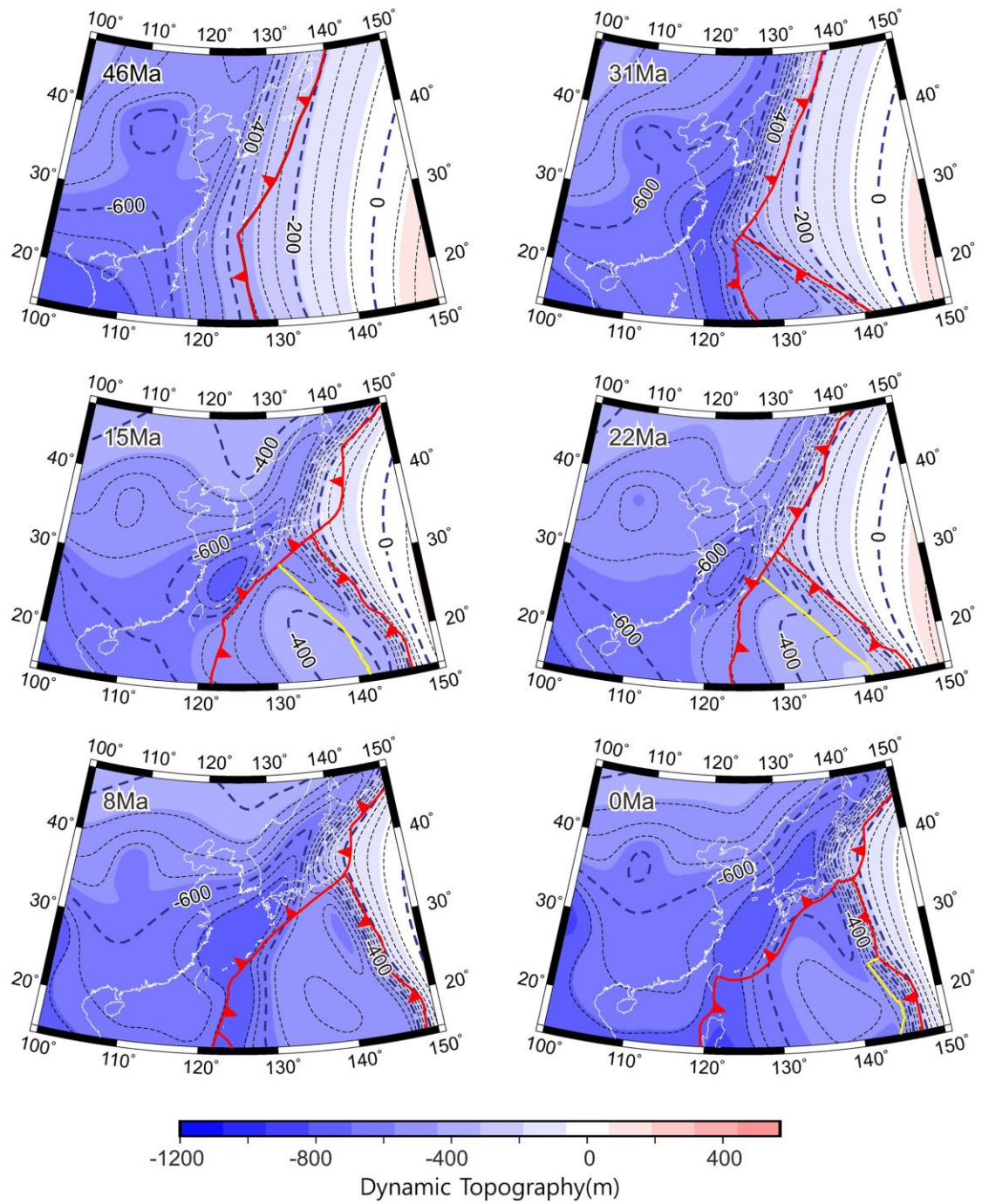


Figure 4. Maps showing the evolution of the dynamic topography predicted by Case 1 - 1. The thick red lines and the thick yellow lines represent subduction zones and faults and sea floor spreading centers, respectively. Coastlines are shown with white lines. The map area and location are the same as those in Figure 1.

6. 东亚夏季风陆地的水汽源-汇网络与相关大气转向



翻译人: 杨会会 11849590@mail.sustech.edu.cn

Cheng T F, Lu M Q. *Moisture Source–Receptor Network of the East Asian Summer Monsoon Land Regions and the Associated Atmospheric Steerings*[J]. *Journal of Climate*, 2020, 9213–9231

<https://doi.org/10.1175/JCLI-D-19-0868.1>

摘要: 本研究旨在构建一个新的水汽源-汇 (S-R) 网络来研究与东亚夏季风环流相关的大气水循环。文章通过动态回收模型 (DRM), 对东亚季风区 6 个陆地地点的湿季 (4–9 月) 降雨的 68%–74% 进行了定性分析。结果表明, 对东亚下游的几个水汽汇集区而言, 其水汽来自于陆地水汽源的可能性与来自海洋水汽的可能性相同或更大。陆地水汽源区如印度次大陆、印度支那、中国西南和青藏高原东部地区, 是由西南季风降雨维持供给的, 并对下游东亚区域的降水有相当大的贡献。此外, 在雨季的前期和后期, 下游水汽汇集区的西南水汽源和东南水汽源交替主导了水汽供应, 即“SW-SE 源摆动”。这一源-汇网络主要受北太平洋副热带高压和热带气旋的纬向振荡控制。对耦合环流的了解可能有助于受其影响的源-汇的强度的预测。值得注意的是, 印度次大陆和青藏高原的水汽供应增加与来自俄罗斯西部的高空波列有很好的相关性。最后, 前一个冬季的 El Niño 现象可能有利于 (抑制) 西南 (东南) 源在下一个雨季的水汽贡献。研究结果为了解东亚夏季风的水循环及其控制环流提供了思路, 并强调了上风向陆地水汽源在下风向降水和淡水资源中的作用。

ABSTRACT: This study aims to construct a novel source–receptor (SR) network to study the atmospheric water cycle associated with the East Asian summer monsoon (EASM) circulation. Using a dynamical recycling model (DRM), 68% – 74% of the wet season (April–September) precipitation in six EASM land regions is attributed. The results reveal that terrestrial sources can be equally or more competitive than oceans for several sink regions downwind in East Asia. Terrestrial sources, such as the Indian subcontinent, Indochina, Southwest China, and the eastern Tibetan Plateau, are sustained by southwesterly monsoons and contribute to appreciable fractions of precipitation in the East Asian subregions downwind. Further, southwesterly and southeasterly sources for a sink region alternately dominate the moisture supply in the early and late wet season,

respectively, referred to as the “SW–SE source swing.” The SR network is found to be largely governed by the zonal oscillation of the western North Pacific subtropical high and tropical cyclones. Knowledge about the coupled circulations might promise more predictability of the strength of the affected SR pairs. Notably, enhanced moisture supplies from regions such as the Indian subcontinent and Tibetan Plateau are well correlated with an upper-level wave train from western Russia. Finally, the preceding wintertime El Niño may favor (suppress) the moisture contribution of southwesterly (southeasterly) sources in the following wet season. The findings offer insights into the EASM water cycle and the governing circulations, and also accentuate the role of upwind terrestrial sources in the downwind precipitation and freshwater resources.

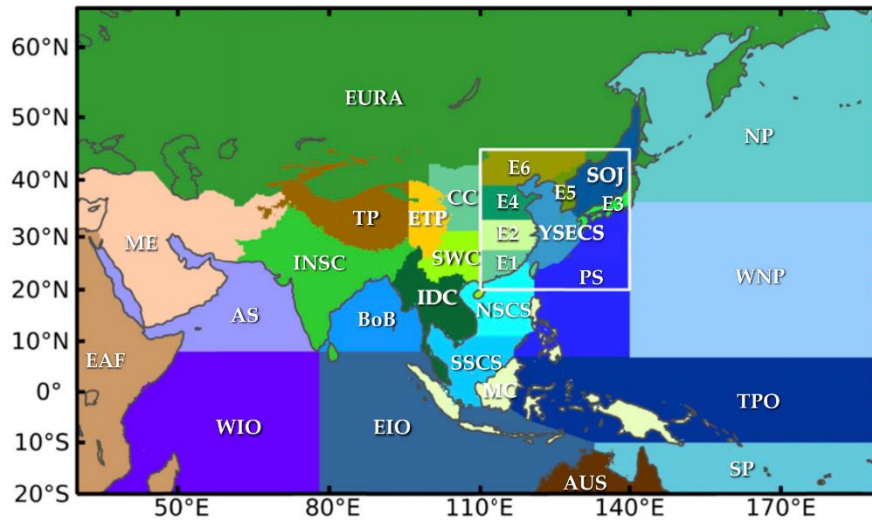


Figure 1. The prescribed 30 regions in the study domain. The labels E1–E6 denote the sink regions within the EASM region (outlined in white). Source regions include Eurasia (EURA), the Middle East (ME), eastern Africa (EAF), the Arabian Sea (AS), the western and eastern Indian Ocean (WIO, EIO), the Indian subcontinent (INSC), the Bay of Bengal (BoB), the Tibetan Plateau (TP), the eastern Tibetan Plateau (ETP), central China (CC), Southwest China (SWC), Indochina (IDC), the northern and southern South China Sea (NSCS, SSCS), the Maritime Continent (MC), Australia (AUS), the Yellow Sea and East China Sea (YSECS), the Sea of Japan (SOJ), the Philippine Sea (PS), the North Pacific (NP), the western North Pacific (WNP), the tropical Pacific Ocean (TPO), and the South Pacific (SP). The Tibetan Plateau is defined as topography with altitude reaching 3 km or above.

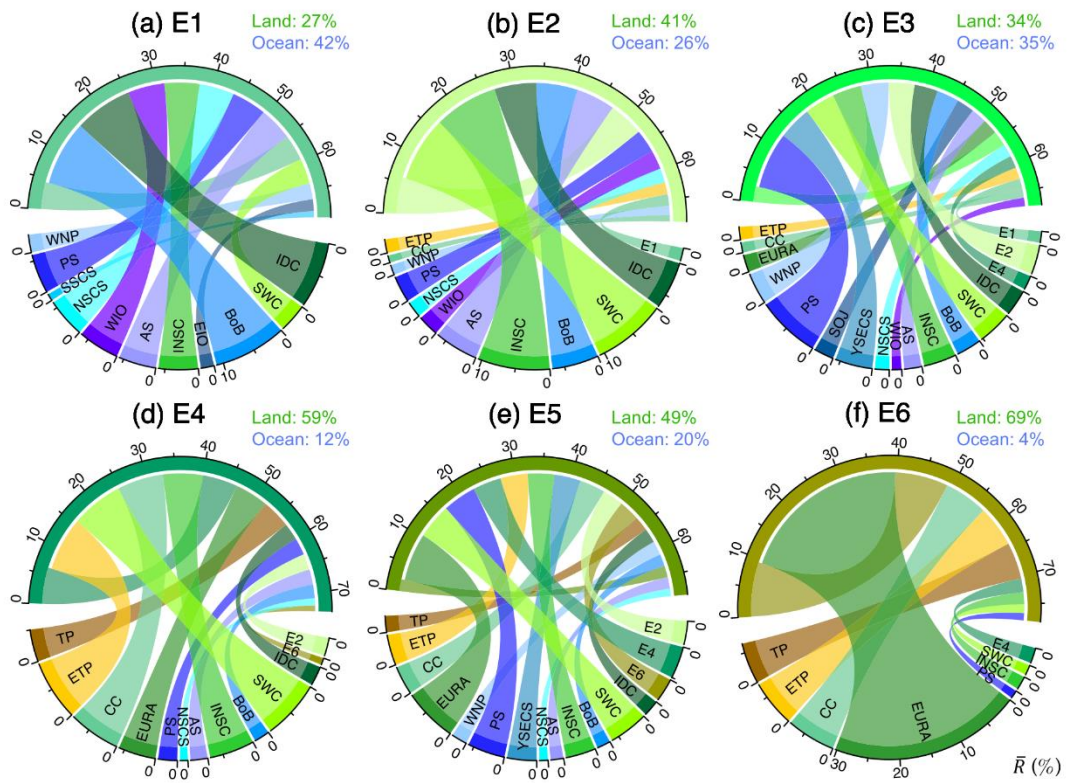


Figure 2. Wet season climatology of the ratio contribution (%) for each source to the (a)–(f) E1–E6 regions, respectively. Sources with the ratio contribution less than 1% are omitted in the chord diagram. The ratio contributions of land and ocean sources are given at the top right of each panel, capped by the total ratio of precipitation attributed by the model. The coloring matches that in Figure. 1 for easy reference.

7. 测试海水中钙浓度的变化对浮游有孔虫中其他元素/钙比的影响： 利用培养实验



翻译人：王浩森 11930841@mail.sustech.edu.cn

Le Houedec S, Erez J, Rosenthal Y. Testing the Influence of Changing Seawater Ca Concentration on Elements/Ca Ratios in Planktic Foraminifera: A Culture Experiment.[J] Geochemistry, Geophysics, Geosystems, 2021, 22: e2020GC009496.

<https://doi.org/10.1029/2020GC009496>

摘要：有孔虫壳中的元素/钙比值常用于评估海洋的物理化学性质（例如古温度，古 pH 值……）。在地质时间尺度上，这些参数也可能取决于海水化学成分的变化。本文研究了改变海水中 Li / Ca, Mg / Ca, Sr / Ca, B / Ca 和 Na / Ca 比值对浮游有孔虫 *Globigerinella siphonifera* 的低镁方解石外壳的影响。具体而言，我们推断浮游有孔虫壳中的 Na / Ca 可能指示过去海洋中 Ca 浓度。由于当今海水中的 Ca 浓度相对于盐度在很大程度上是保守的，因此无法进行区域的校准。因此，我们在恒定温度（25° C）和两个盐度（37 和 40.6）下，利用变化的 Casw（10.5 – 29 mmol / kg）培养了从埃拉特湾（红海）收集的浮游有孔虫（*G. siphonifera*）。当改变生长培养基的 Casw 时，壳中 Mg / Ca 和 Na / Ca 之间的关系以及它们在海水中的对应变化最适用于隐含幂分布系数函数的幂函数来描述。对于 Sr / Ca 和 Li / Ca，壳和海水之间的关系由与原点相交的线性函数表示，这指示它们的分布系数对 Casw 的变化不敏感。结果还证实，有孔虫 B / Ca 不受海水 Casw 的影响。我们得出结论，浮游有孔虫中的 Na / Ca 比值可以作为新生代海洋中 Ca 的可靠替代物，并且其他 El / Ca 比值可以用来确定其相对于 Ca 的过去浓度。

ABSTRACT: Element/Ca ratios in foraminifera shells are used to assess oceanic physical-chemical properties (e.g., paleo-temperature, paleo-pH...). On geological time scales, these proxies may also depend on changes in the chemical composition of seawater. Here we investigate the effect of changing seawater calcium concentration on the Li/Ca, Mg/Ca, Sr/Ca, B/Ca, and Na/Ca ratios in low-Mg calcite shells of the planktic foraminifer *Globigerinella siphonifera*. Specifically, we evaluate the possibility that Na/Ca in planktic foraminifera shells may serve as a proxy for Ca

concentrations in the past ocean. Since Ca concentration in today's open ocean is largely conservative with relation to salinity, field calibrations are not possible. Therefore, we cultured the planktic foraminifer (*G. siphonifera*) collected from the Gulf of Eilat (Red Sea) in variable Casw (10.5–29 mmol/kg), at constant temperature (25°C) and under two salinities (37 and 40.6). When changing the Casw of the growth medium, the relationships between Mg/Ca and Na/Ca in the shells and their corresponding ratios in the seawater are best described by power functions implying a variable distribution coefficient function. For Sr/Ca and Li/Ca, the relations between the shells and the seawater are described by linear functions intersecting the origin implying their distribution coefficients are insensitive to changes in Casw. The results also confirm that foraminiferal B/Ca is not influenced by seawater Casw. We conclude that Na/Ca ratios in planktic foraminifera may serve as reliable proxy for Cenozoic ocean Ca, and that other El/Ca ratios may be used to determine their past concentrations relative to Ca.

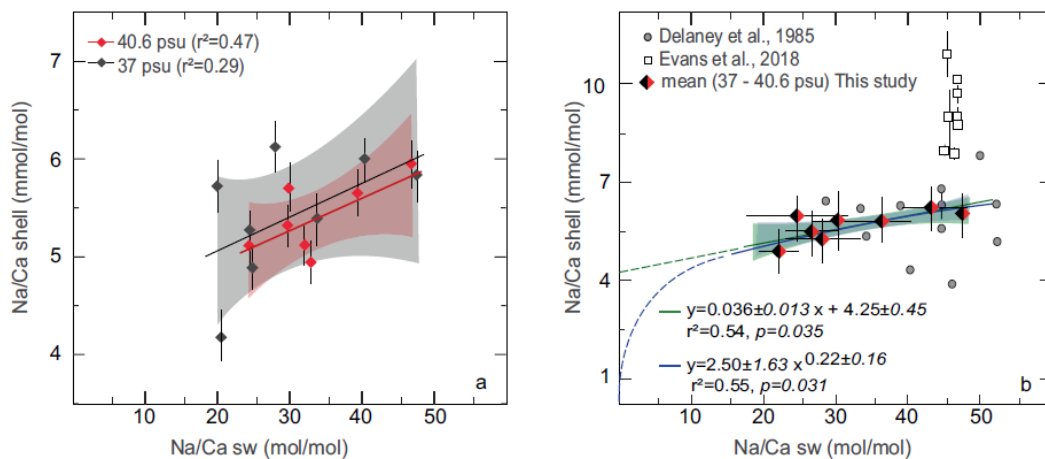


Figure 1. Na/Ca ratios of cultured *Globigerinella siphonifera*. (a) Na/Ca shell versus Na/Ca sw of *G. siphonifera*. The shaded areas represent the 95% confidence level of the fit function. (b) Compiled record from cultured planktic foraminifera under variable Na/Ca seawater ratio. Note that the data of Delaney et al. (1985) were obtained for *G. sacculifer* and Evans et al. (2018) from *G. ruber*, the latter were obtained from LA-ICP MS. Both linear and the power fit are represented in blue and green, respectively, and the shaded areas represent the 95% confidence level on the fit of *G. siphonifera*. In the panels, the error bars on our data integrate uncertainty due to the mass correction and the ICP analytical standard deviation.

8. 地中海东部地磁场异常的发生方向：来自塞浦路斯的新数据与突变方向

翻译人：曹伟 11930854@QQ.com



Tema E, Hedley I, F.J. Pavón-Carrasco, et al. The directional occurrence of the Levantine geomagnetic field anomaly: New data from Cyprus and abrupt directional changes [J]. Earth and Planetary Science Letters, 2021, 557:116731.

<https://doi.org/10.1016/j.epsl.2020.116731>

摘要：通过对塞浦路斯及附近国家新的和以前发表的定向古地磁数据分析，我们对地中海东部铁器时代异常（LIAA）的发生方向提出了新的见解。新的方向是从公元前 2000 年至 1400 年塞浦路斯五处考古遗址的小壁炉和烤箱等原位烘烤粘土结构获得的，这些新方向的定义非常明确，并被添加到塞浦路斯缺少的参考数据集中。我们利用这些新记录和附近国家的文献资料，研究了地中海东部和中东地区地磁场的方向变化，使用塞浦路斯、以色列、土耳其和叙利亚的重要参考数据，计算出中东地区第一个古方向长期变化曲线。这条曲线覆盖了过去四千年时期，显示了几个以方向突变为特征的周期。在公元前 900 年左右可以清楚地观察到曲率的最大变化，其特征是高达每世纪 13.2 次的变化频率。新曲线证实，在以极端强度值为显著特征的地中海东部铁器时代异常期间，地磁场也具有陡倾和重要的方向变化特征。最大曲率从公元前 10 世纪和公元前 8 世纪左右在地中海东部观察到的两个飘移了大约一个世纪的明显强度峰值。其他重要的曲率变化时期也被确定，值得进一步研究。

ABSTRACT: We present new insights on the directional occurrence of the Levantine Iron Age Anomaly (LIAA) through the analysis of new and previously published directional archaeomagnetic data from Cyprus and nearby countries. The new directions, obtained from in situ baked clay structures such as small hearths and ovens from five Cypriot archaeological sites, dated from 2000 BCE to 1400 CE, are very well defined and are added to the scant reference dataset for Cyprus. The new records together with literature data from nearby countries are used to investigate the directional variations of the geomagnetic field in the Eastern Mediterranean and Middle East. The

first directional palaeosecular variation curve for Middle East is calculated using a critical selection of reference data from Cyprus, Israel, Turkey and Syria. The curve covers the last four millennia and shows several periods characterized by abrupt directional changes. A maximum change in curvature is clearly observed around 900 BCE, characterized by a change rate as high as 13.2 per century. The new curve confirms that during the Levantine Iron Age Anomaly notable for extreme intensity values, the geomagnetic field was characterized by steep inclinations and important directional change too. The maximum curvature is shifted by around one century from the two distinct intensity spikes previously observed in Levant around the 10th and 8th centuries BCE. Other periods of important curvature change are also identified and deserve further investigation.

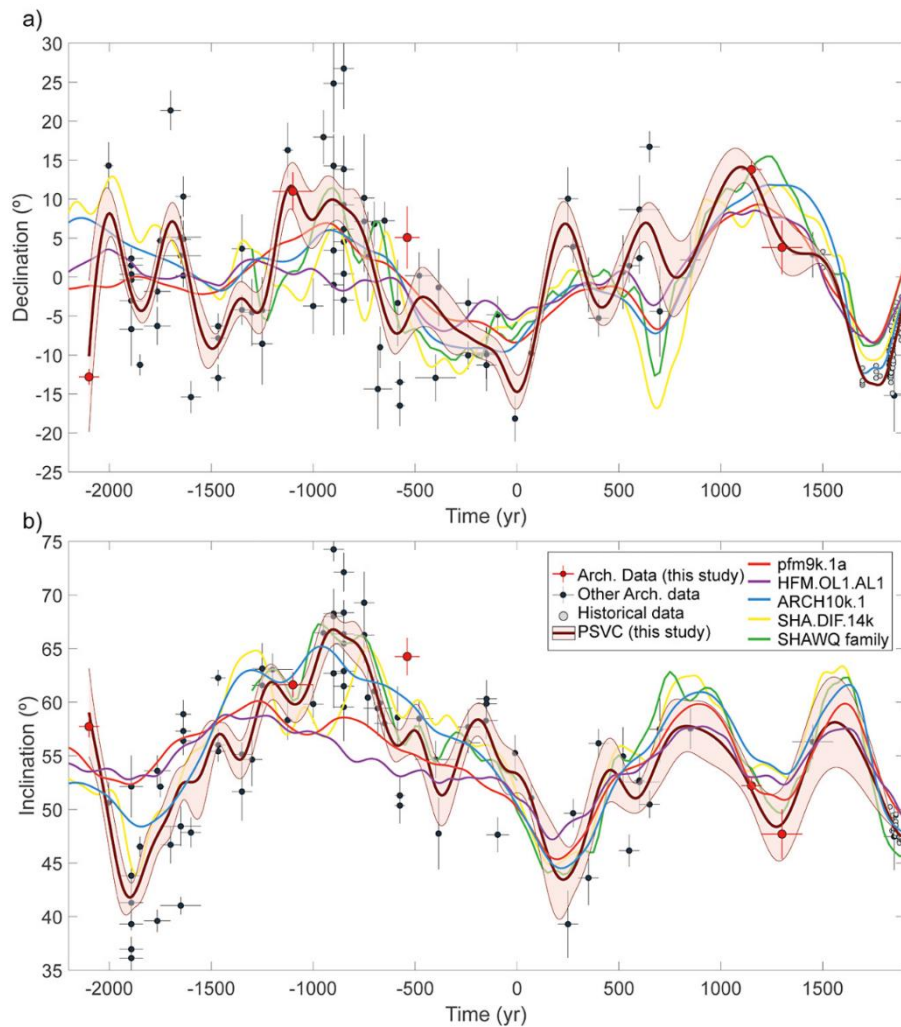


Figure 1. New palaeosecular variation curves for a) declination and b) inclination for the Eastern Mediterranean (dark red curves with error bands at 1 sigma of probability). Black and grey dots represent the archaeomagnetic and historical data, respectively. Different color curves show the global model predictions.

9. 地磁场强度与白垩纪正极性超时：来自哥斯达黎加的新结果

翻译人：张伟杰 12031188@mail.sustech.edu.cn



Di Chiara A, Tauxe L, et al. Earth's magnetic field strength and the Cretaceous Normal Superchron: New data from Costa Rica. Geochemistry, Geophysics, Geosystems. 2021.

<https://doi.org/10.1029/2020GC009605>

摘要：约束地球磁场强度的长期变化和平均值是理解地磁场特征和行为的基础。由于关键时段内的数据存在差异，以至于地磁场的平均强度以及强度和反转频率之间的关系仍然存在问题。本文，我们聚焦于白垩纪正极性超时（CNS，121-84Ma），在这段时期内没有发生地磁场倒转。我们报告了来自哥斯达黎加 Nicoya 半岛与 Murcièlago 岛 41 个海底玄武玻璃采点的新结果。新的和修订过的 $^{40}\text{Ar}/^{39}\text{Ar}$ 与来自之前的生物地层年龄约束指示它们的年龄从 141 至 65 Ma。一个年龄为 135.1 ± 1.5 Ma (2σ) 的采样点得到了一个 34 ± 8 μT 的可靠的强度结果（相应的虚轴向偶极矩为 88 ± 20 ZAm²），从 121 到 112 Ma 三个 CNS 开始阶段的采样点得到的古强度结果从 21 ± 1 至 34 ± 4 μT （虚轴向偶极矩从 53 ± 3 至 87 ± 10 ZAm²）。这些来自 CNS 期间的结果均高于 ~ 42 ZAm² 的长期平均结果以及来自蒙古 Suhongtu 的 46-53ZAm² 的结果，与塞浦路斯 Troodos 蛇绿岩的 81 ZAm² 结果相似（本研究重新解释）。新的哥斯达黎加的结果与重新解释的数据一起，表明在 CNS 开始之前和之后，地磁场的强度大致相同。因此，这些数据不支持极性间隔长度和磁场强度之间的严格相关性。

ABSTRACT: Constraining the long-term variability and average of the Earth's magnetic field strength is fundamental to understanding the characteristics and behavior of the geomagnetic field. Questions remain about the strength of the average field, and the relationship between strength and reversal frequency, due to the dispersion of data from key time intervals. Here, we focus on the Cretaceous Normal Superchron (CNS; 121-84 Ma), during which there were no reversals. We present new intensity results from 41 submarine basaltic glass (SBG) sites collected on the Nicoya Peninsula and Murcièlago Islands, Costa Rica. New and revised $^{40}\text{Ar}/^{39}\text{Ar}$ and biostratigraphic age constraints from previous studies indicate ages from 141 to 65 Ma. One site with an age of $135.1 \pm$

1.5 Ma (2σ) gave a reliable intensity result of $34 \pm 8 \mu\text{T}$ (equivalent to a virtual axial dipole moment, VADM, value of $88 \pm 20 \text{ ZAm}^2$), three sites from 121 to 112 Ma, spanning the onset of the CNS, vary from 21 ± 1 to $34 \pm 4 \mu\text{T}$ (53 ± 3 to $87 \pm 10 \text{ ZAm}^2$). These results from the CNS are all higher than the long-term average of $\sim 42 \text{ ZAm}^2$ and data from Suhongtu, Mongolia ($46\text{-}53 \text{ ZAm}^2$) and are similar to the Troodos Ophiolite, Cyprus (81 ZAm^2 , reinterpreted in this study). Together with the reinterpreted data, the new Costa Rica results suggest that the strength of the geomagnetic field was approximately the same both before and after the onset of the CNS. Therefore, the data do not support a strict correlation between polarity interval length and the strength of the magnetic field.

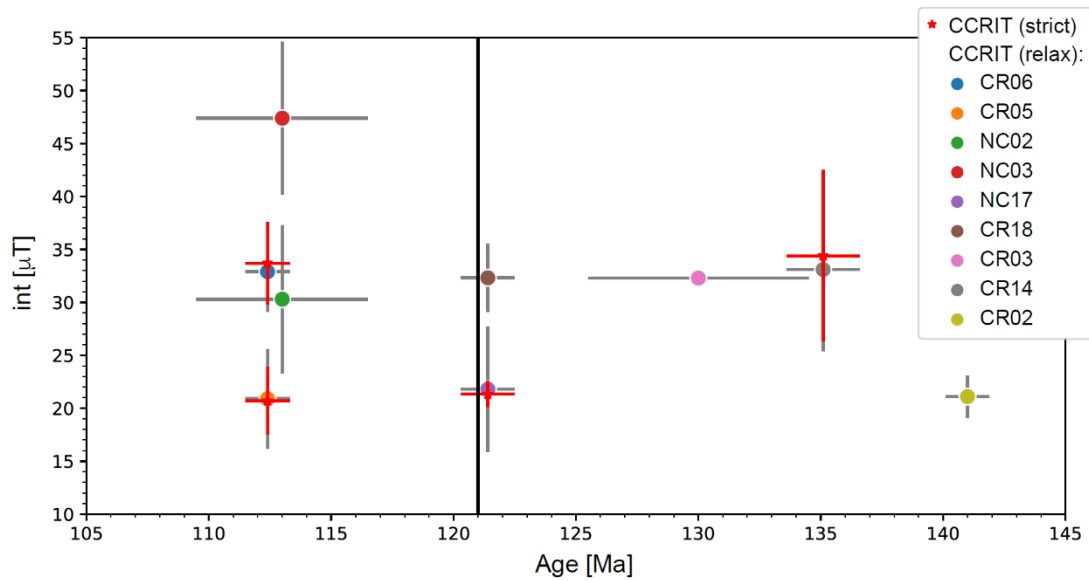


Figure 1. Paleointensity data (in μT) with 1σ error bars from Costa Rica sites vs. $^{40}\text{Ar}/^{39}\text{Ar}$ ages (in Ma) with 2σ error bars. Red stars are the sites for which the paleointensity values were obtained using the CCRIT-strict selection criteria. The CNS onset interval is marked with a vertical black line.

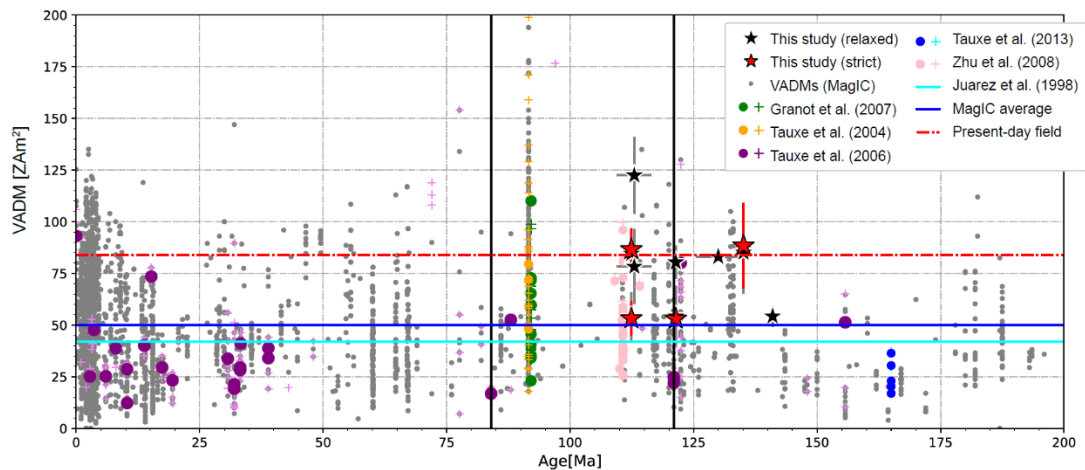


Figure 2. VADM (in ZAm^2) vs age (Ma). The black and red stars are the results of this Costa Rica study

obtained using the CCRIT-relaxed and -strict selection criteria, respectively, with 1σ error bars and ^{40}Ar - ^{39}Ar ages with 2σ error bars. Grey dots represent the virtual (axial) dipole moments ($V[A]DM$) available from the MagIC database spanning the last 200 Ma. The bounds of the Cretaceous Normal Superchron (CNS) are indicated with vertical black lines. The strength of the present dipole field is shown as a dashed red line, the solid blue line represents the average of all the MagIC data, and the long-term average from Juarez and Tauxe (2000), and Tauxe et al. (2013) is shown as a solid aquamarine line. Circles represent the data from SBGs that we re-analyzed using the same CCRIT criteria as employed in our study, while the original literature data as presented by the authors are marked as crosses.

10. 由湖泊沉积物重建全新世以来东格陵兰岛 Renland 冰盖的演化史



翻译人：李海 12031330@mail.sustech.edu.cn

Medford, A.K, Hall, B.L, Lowell, T.V, et al. *Holocene glacial history of Renland Ice Cap, East Greenland, reconstructed from lake sediments [J]. Quaternary Science Reviews, 2021, 258, 106883.*

<https://doi.org/10.1016/j.quascirev.2021.106883>

摘要：冰川萎缩、永久冻土的融化以及海冰的减少，都表明北极冰冻圈响应当今气候变暖的快速收缩，这一趋势即便不加速也将持续下去。北极冰冻圈对过去气候变化的响应可以指示当前和未来的变化。作者研究了 12000 年以来与东格陵兰岛 Renland 冰盖相关的冰川波动和融水变化记录，包括从全新世早期一直至今的小冰期降温的记录。湖泊沉积物记录表明，全新世早期冰川融化迅速，9500 yr BP 左右的冰川范围可能比现在还小。全新世早期至 7500 yr BP 之间，冰川活动造成研究的湖泊中存在沉积岩粉。~7000 - 4000 yr BP 的大部分时间内没有沉积岩粉，指示冰盖的范围比现在还小。然而，在这一时期，蓝灰色黏土薄层可能指示了千年尺度的冰盖扩张，Renland 冰盖在寒冷期的范围与现今相似。全新世晚期（3200~3400 yr BP）再次发生冰川沉积，在 1340 yr BP 左右为短暂的冰川期，约在 1050 yr BP 后发生一次重大事件。作者认为，在上个千年里，湖中沉积岩粉的沉积与 Renland 冰盖向小冰期位置的扩张方向一致，其标志是一个新的灰色沉积偏移。放射性碳年代测定结果指示 500 年前存在一个相对短暂的暖期，当时的冰盖与公元 2011 的范围相似，而后冰盖继续扩张。Renland 冰盖的演化的模式与该区其他冰盖类似，但也存在较大差异，Scoresby Sund 等低纬度地区的冰盖可能未记录全新世中期的信息。因此，细致的地理和地貌环境调查对全面了解该区的冰盖变化具有重要意义。

Abstract: Shrinking glaciers, melting permafrost, and reduced sea ice all indicate rapid contraction of the Arctic cryosphere in response to present-day climate warming, a trajectory that is expected to continue, if not accelerate. The reaction of the Arctic cryosphere to past periods of climate variation can afford insight into its present and future behavior. Here, we examine a ~12,000 year record of glacier fluctuations and meltwater variation associated with the Renland Ice Cap, East Greenland, that extends from the early Holocene thermal optimum through the cooling of the Little Ice Age to present. Sediment records from glacially fed lakes indicate rapid early Holocene deglaciation, with ice extent likely slightly smaller than at present by ~9500 yr BP. Glacial activity resulted in occasional deposition of rock flour in the studied lakes in the early Holocene until at least ~7500 yr BP. Rock flour is absent for much of the

period ~7000 - 4000 yr BP, suggesting ice extent generally was smaller than at present. However, thin layers of blue-gray clay throughout this period may indicate millennial-scale ice expansions, with Renland Ice Cap briefly reaching extents during cold phases that may have been similar to today. Glacial sediment deposition occurred again in the late Holocene at ~3200 - 3400 yr BP and was followed by a brief glacial episode at ~1340 yr BP and then a major event beginning shortly after ~1050 yr BP. We infer that rock flour deposition in the lakes in the last millennium corresponds with advance of Renland glaciers to their Little Ice Age positions, marked by a fresh, gray drift limit. Radiocarbon dates of in situ plant remains adjacent to the present ice cap indicate a short relatively warm period ~500 yr ago, when ice was within its AD 2011 limit, followed by glacier readvance. The general pattern of ice fluctuations in Renland is similar to that at other ice caps in the region, but also has important differences, including the preservation of a possible mid-Holocene record at times when lower-elevation ice caps in the Scoresby Sund region may have been absent. This finding reinforces the concept that examination of multiple geographic and geomorphologic settings is necessary for a full understanding of ice variations in a region.

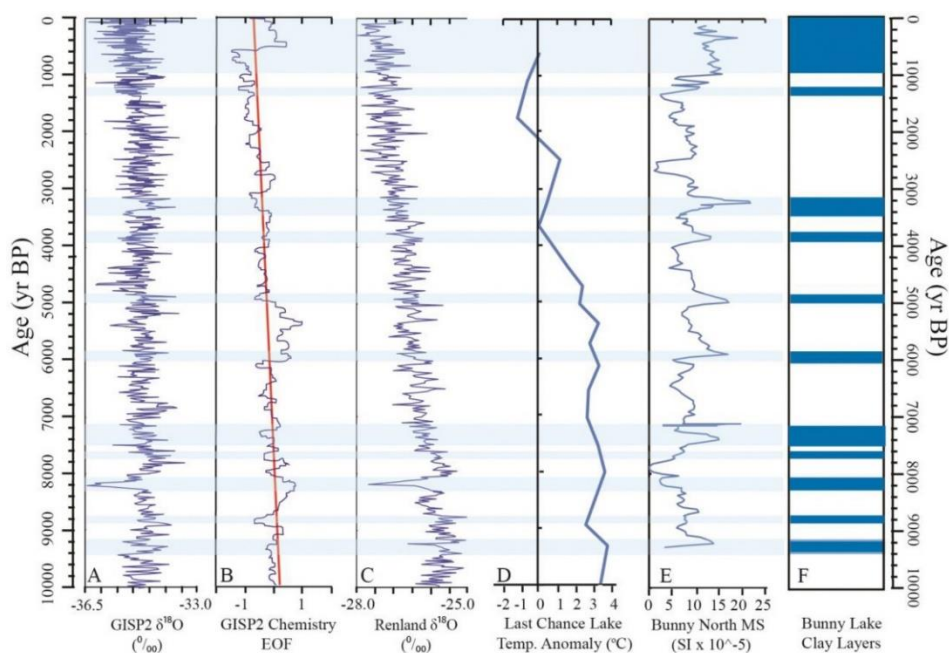


Figure. 1. Comparison of the Renland lake record with regional climate proxies. A. GISP2 $\delta^{18}\text{O}$ profile (Grootes and Stuiver, 1997); B. GISP2 chemistry data as represented by an empirical orthogonal function (O'Brien et al., 1995); C. Renland ice core $\delta^{18}\text{O}$ profile (Vinther et al., 2008); D. Temperature anomaly relative to preindustrial values inferred from chironomids in Last Chance Lake, Milne Land (Axford et al., 2017); E. Magnetic susceptibility record - a proxy for glacial sediment input - from the north basin of Bunny Lake; F. Chronology of the visible inorganic clayey-silt layers in Bunny Lake indicated by blue lines. (For interpretation of the references to color in this Figure legend, the reader is referred to the Web version of this article.)

11. Ranau 和 Telupid (马来西亚沙巴洲) 超基性岩锆石 U-Pb 年龄和 Lu-Hf 同位素: 对东南亚的构造演化的启示



翻译人: 周洋 zhouy3@sustech.edu.cn

Basilios Tsikouras, Chun-Kit Lai, Elena Ifandi et al. New zircon radiometric U-Pb ages and Lu-Hf isotopic data from the ultramafic-mafic sequences of Ranau and Telupid (Sabah, eastern Malaysia): Time to reconsider the geological evolution of Southeast Asia? [J]. Geology, 2021, v. 49.

<https://doi.org/10.1130/G48126.1>

摘要: 来自 Ranau 附近的橄榄岩和马来西亚东部沙巴地区 Telupid 蛇绿岩之前被认为是侏罗-白垩纪的年龄, 沙巴的镁铁质-超镁铁质岩主要是蛇绿岩。现在研究认为, 这些岩石是在中新世 (9.2-10.5 Ma) 的一次岩浆事件中形成的, 被解释为 Ranau 次大陆橄榄岩在伸展过程中形成, 同时发生海底扩张形成了更南部的 Telupid 蛇绿岩。Ranau 橄榄岩中具有白垩纪、泥盆纪和新元古代老锆石, 锆石 Lu-Hf 同位素表明它们来自亏损地幔。但是与原始地幔储库相比, 它们含有很大比例的地壳成分, 具有较低的 Hf。地壳成分的加入, 与我们解释的 Ranau 橄榄岩的大陆构造背景以及 Telupid 蛇绿岩形成于狭窄的弧后盆地一致。我们推断在中新世, Sulu 海可能已经从西南延伸到沙巴中部。由于 Celebes 海向 Sabah 之下俯冲, 导致 Sulu 弧分裂、垮塌, 在这一过程中形成 Telupid 洋壳。Sulu 弧是地壳物质参与 Telupid 蛇绿岩锆石演化的潜在来源。

ABSTRACT: New zircon U-Pb geochronology from a peridotite suite near Ranau and the Telupid ophiolite in Sabah, eastern Malaysia, contradict previous studies, which assumed that the Sabah mafic-ultramafic rocks are largely ophiolitic and Jurassic–Cretaceous in age. We show that these rocks formed during a magmatic episode in the Miocene (9.2–10.5 Ma), which is interpreted to reflect infiltration of melts and melt-rock reaction in the Ranau subcontinental peridotites during extension, and concurrent seafloor spreading forming the Telupid ophiolite further south. Older zircons from the Ranau peridotites have Cretaceous, Devonian, and Neoproterozoic ages. Zircon Lu-Hf isotopic data suggest their derivation from a depleted mantle. However, significant

proportions of crustal components have been incorporated in their genesis, as evidenced by their less-radiogenic Hf signature compared to a pristine mantle reservoir. The involvement of a crustal component is consistent with our interpreted continental setting for the Ranau peridotite and formation in a narrow backarc basin for the Telupid ophiolite. We infer that the Sulu Sea, which was expanding throughout much of the Miocene, may have extended to the southwest into central Sabah. The Telupid oceanic strand formed during the split, collapse, and rollback of the Sulu arc due to the subduction of the Celebes Sea beneath Sabah. Incorporation of the Sulu arc in the evolving Miocene oceanic basin is a potential source to explain the involvement of crustal material in the zircon evolution of the Telupid ophiolite.

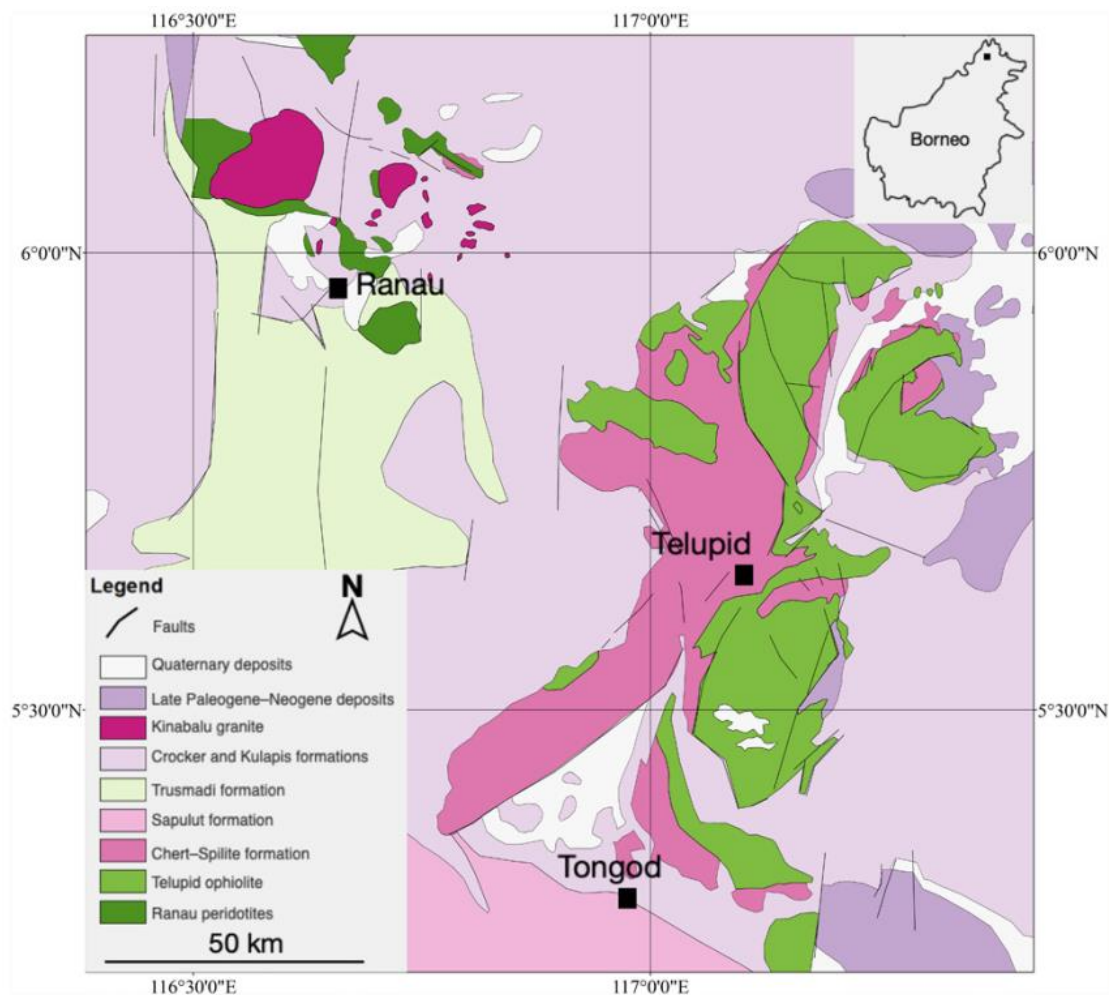


Figure 1. Simplified geological map of central Sabah, eastern Malaysia, compiled from Yin (1985), Tongkul (1997), and our observations.

12.对风化的玄武岩岩脉进行地磁测量和磁化率测绘揭示土壤蠕变与扰动



翻译人: 张琪 zhangq7@sustech.edu.cn

Tio von Dobeneck T, Müller M, Bosbach B, et al. *Ground Magnetic Surveying and Susceptibility Mapping Across Weathered Basalt Dikes Reveal Soil Creep and Pedoturbation*. [J]. *Frontiers in Earth Science*, 2021, 8, 682.

<https://doi.org/10.3389/feart.2020.592986>

摘要: 对沉积岩中的风化基性岩墙进行地表磁测,不仅可以确定席状玄武岩侵入的走向、宽度和埋藏深度,而且可以反映其粘土风化产物的深部变形。我们以德国中部黑尔德堡岩墙群为例来说明这一发现及其在地貌学中的实际适用性,在该岩墙群中,蓝色和橄榄灰色的玄武岩衍生粘土不仅继承了以前被玄武岩占据的岩墙空间,而且还继承了其大部分磁性矿物以及其强烈的剩磁。这种韧性玄武岩“标记土”会随着周围的低磁性土壤变形和移动,但仍可通过强烈的颜色反差和强磁化率对其进行辨别。地磁测量可以描绘米级精度的土壤蠕变和深度为分米级精度的玄武岩风化。对一个探槽里的风化岩墙横截面进行现场磁化率测绘,可以详细分析其过去的土壤变形。风化和泥流使简单的岩墙“垂直片状”异常变成复杂但仍然可以解释的复合模式,这为野外土壤蠕变和土壤扰动研究提供了一个新的且有前景的探索性的方法。

ABSTRACT: Ground magnetic survey profiles across a soil-covered and weathered mafic dike in sedimentary host rock not only permit to delineate the strike, width and burial depth of the intrusive basalt sheet, but also reflect the subsurface deformation of its clayey weathering products. We illustrate this finding and its practical geomorphological applicability by an example from the mid-German Heldburg Dike Swarm, where blue- and olive-gray basalt-derived clays inherited not just the dike space previously occupied by the basalt, but also large parts of its magnetic iron minerals and their strong induced and remanent magnetization. Such ductile basaltic “marker soils” deform and move with the surrounding low-magnetic host soils, but remain distinguishable by their contrasting colors and high magnetic susceptibility. Ground magnetic surveys can therefore delineate soil creep distance at meter-

and basalt weathering depth at decimeter-precision. Magnetic mapping of a weathered dike's cross-section from an exploration trench by in-situ susceptometry permits to analyze past soil deformation in great detail. Weathering and solifluction transforms the simple "vertical sheet" anomalies of dikes into complex, but still interpretable composite patterns, providing a new and promising exploratory approach for field studies concerned with soil creep and pedoturbation.

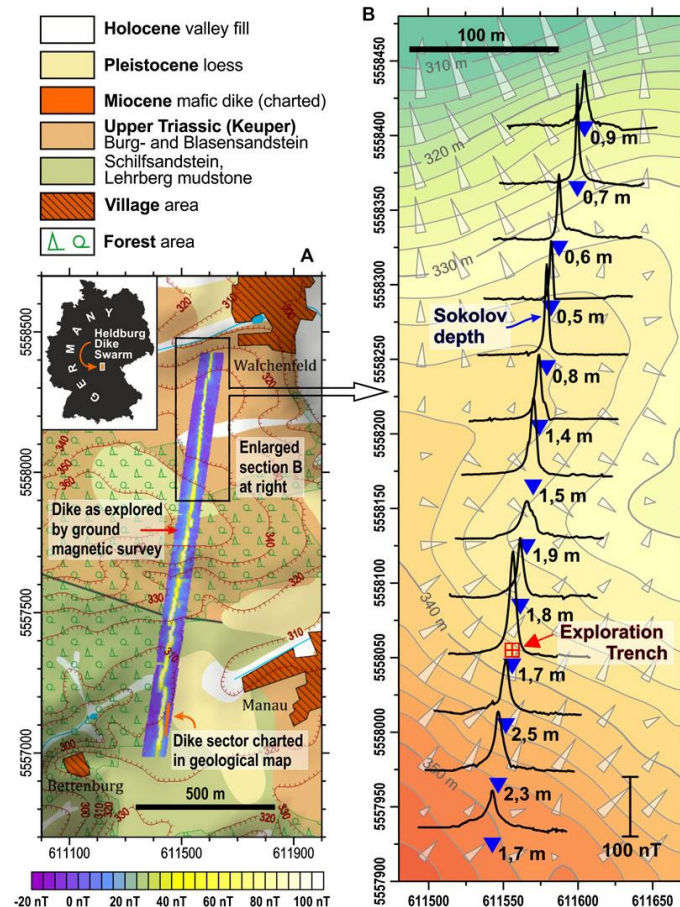


Figure 1. (A) Inset: The Heldburg Dike Swarm (HDS) region is located in the mid-German Upper Triassic "Keuper" formations. Previously charted sector (orange line) and newly explored complete course (magnetic anomaly map in blue/yellow) of a weathered mid-Miocene basalt dike near the villages of Manau and Walchenfeld (Hassberge, Northern Bavaria). The shown geological map is redrawn from Schröder (1976) and georeferenced to UTM coordinates (WGS 84 sector 32N). (B) Northern dike section delineated by 13 precision ground magnetic W-E profiles. Note the varying amplitudes and shoulders of the anomaly. Blue triangles and numbers mark dike center positions and Sokolov depth estimates. The red square symbolizes the position of the exploration trench. Topographic contour lines are based on own GPS elevation data; gray arrows mark slope gradients.

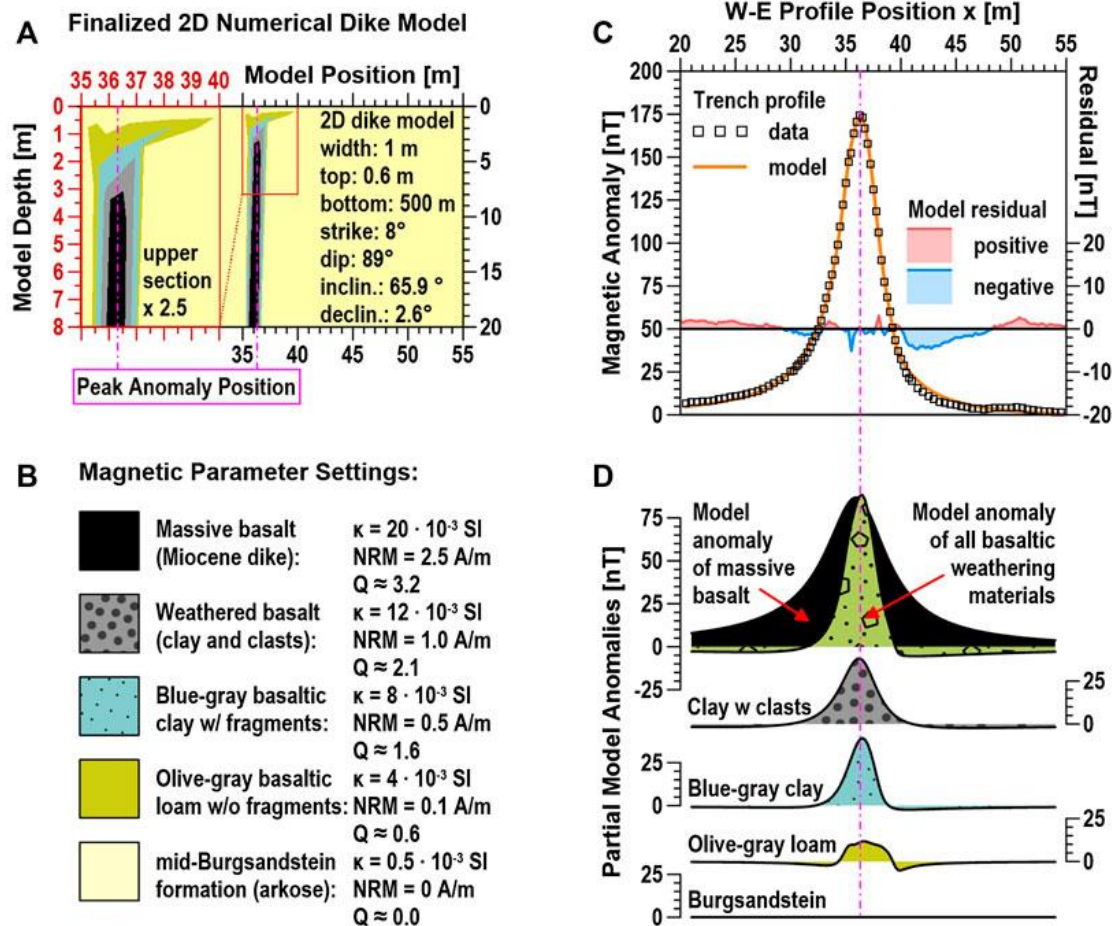


Figure 2. (A) 2D model of weathered HDS dike based on the simplified and extrapolated exploration trench section of Figure 2. Shown at left (red axes) is a 2.5x enlarged view of the dike top; the smaller model at right (black axes) is scaled proportionally with Figure 3C. (B) Distinguished model materials, their color patterns and magnetic properties. (C) Total 2D dike model anomaly (orange line) and corrected ground magnetic survey anomaly data (squares) with model residuals (note vertical offset and expanded scaling of residual axis). (D) 2D model-based partial magnetic anomalies of pristine basalt (black), all weathering materials (olive green), and specific anomaly contributions by each material classified in Figure 3B. All anomaly axes are equivalently scaled in nT.